

**Cool Under the Spotlight: Inferring the Photospheric Temperature of
Betelgeuse from Optical Spectroscopy**

A Thesis

Presented to the

Faculty of

San Diego State University

In Partial Fulfillment

of the Requirements for the Degree

Master of Science in Astronomy

by

Robert Steven Baldocchi, Jr.

Summer 2022

SAN DIEGO STATE UNIVERSITY

The Undersigned Faculty Committee Approves the

Thesis of Robert Steven Baldocchi, Jr. :

Cool Under the Spotlight: Inferring the Photospheric Temperature of Betelgeuse from
Optical Spectroscopy

Douglas Leonard, Chair
Department of Astronomy

Eric Sandquist
Department of Astronomy

Fridolin Weber
Department of Physics

Approval Date

Copyright © 2022
by
Robert Steven Baldocchi, Jr.

DEDICATION

To my parrot and most beloved alarm clock Dio, thank you for your unconditional affection and support.

You know, I'm something of a scientist myself.

– Norman Osborn, Spiderman

ABSTRACT OF THE THESIS

Cool Under the Spotlight: Inferring the Photospheric Temperature of Betelgeuse from
Optical Spectroscopy

by

Robert Steven Baldocchi, Jr.

Master of Science in Astronomy

San Diego State University, 2022

Red Supergiants (RSGs) are high-mass He-burning evolved stars predicted to be the progenitors of Type II-Plateau core-collapse supernovae. Betelgeuse (α Orionis), the most studied Galactic RSG, displayed an unexpected and rapid descent in brightness from October 2019 through March 2020. Its minimum in February 2020 is the deepest recorded for the star. Explanations for this unanticipated event include a dust occultation caused by a prior mass loss event, a drop in the surface temperature of the star, or a combination of the two causes.

We present optical spectroscopy of Betelgeuse using low-resolution spectral data obtained at five epochs during and after the dimming event using the 1-m telescope at Mount Laguna Observatory. The purpose of this thesis is to derive the effective temperature (T_{eff}) of Betelgeuse at all epochs by comparing the equivalent width (W_λ) of the temperature-sensitive 7054 Å line with those measured from PHOENIX synthetic model spectra.

Our analysis finds a strong positive correlation between Betelgeuse's photometric and spectroscopic behavior: Decreases in apparent brightness correlate directly with decreases in inferred temperature, with a globally averaged mean temperature drop of $\Delta T_{eff} = 149 \pm 12$ K inferred during the deepest part of the light-curve minimum compared with the T_{eff} inferred after Betelgeuse had returned to normal brightness. The PHOENIX models predict a decline in V-band magnitude of $\Delta V_{est} = 0.70 \pm 0.04$ from this temperature drop. Compared with the observed dimming of $\Delta V_{obs} = 1.13 \pm 0.03$, this suggests that at least a significant fraction of Betelgeuse's dimming was caused by a T_{eff} change.

Invoking dust from a prior mass-loss event could explain the difference between ΔV_{est} and ΔV_{obs} . However, imaging of Betelgeuse's surface during the Great Dimming revealed an inhomogeneous brightness profile; its southern hemisphere became notably dimmer than the northern hemisphere. Our results, though unable to completely dismiss dust as a contributor, support the conclusion that the observed dimming could have resulted from Betelgeuse's southern hemisphere cooling significantly, $\Delta T \geq 250$ K, while the northern hemisphere maintained a comparatively normal temperature.

TABLE OF CONTENTS

	PAGE
ABSTRACT	vi
LIST OF TABLES	ix
LIST OF FIGURES	x
ACKNOWLEDGMENTS	xiv
CHAPTER	
1 Introduction	1
1.1 Variability in Red Supergiants	4
1.2 Betelgeuse	5
1.2.1 Physical Characteristics	7
1.2.2 Variability	10
1.3 Dimming Episode	14
1.3.1 Pre-Phase Supernova	16
1.3.2 Stellar Winds	17
1.3.3 Variable Photosphere and Radius	17
1.3.4 Dust Occultation	17
1.3.5 Localized Cooling of the Photosphere (No Dust)	19
1.4 Motivation	21
1.5 Spectroscopic Observations	21
2 Methods	26
2.1 Estimating the Effective Temperatures of Red Supergiants	26
2.2 Model Atmospheres and Spectra	29
2.3 Measuring Equivalent Widths	30
2.4 Line Selection and Features	32
2.5 Calibration of the Equivalent Width-Effective Temperature Relation	34
2.6 Establishing a Correlation between V-band Magnitude and Effective Temperature from Models	35
3 Results	40

3.1	Betelgeuse's Effective Temperature Estimated from Observed Spectra	40
3.2	Estimating How V-band Magnitude Changes with Effective Temperature from Models	44
4	Discussion	47
4.1	Analysis	47
4.2	Comparison with Prior Studies.....	47
5	Conclusion	50
5.1	Limitations of this Study and Future Work	50
	REFERENCES	52
	APPENDIX	
	Additional Figures.....	58

LIST OF TABLES

	PAGE
1.1 Atmospheric and Surface parameters for Betelgeuse.	10
1.2 Journal of spectroscopic observations of Betelgeuse obtained at MLO. Displayed are the calendar date, Modified Julian Date (Julian Date - 2400000.5), and estimated V-band magnitude of Betelgeuse at each epoch. Each epoch's V-band magnitude and corresponding uncertainties were derived by averaging over the available AAVSO data in bins of ten days each.	24
1.3 Journal of Spectroscopic Observations of Betelgeuse	25
2.1 Equivalent Widths of the 7054 Å TiO absorption feature measured in PHOENIX MODEL SEDs	33
2.2 Multi-epoch equivalent width measurements of Betelgeuse's 7054 Å TiO absorption feature with uncertainties.	33
2.3 Tabulated values for the standard V-passband sensitivity function for each wavelength λ from Bessell (1990).	37
3.1 Epoch of observation, measured equivalent width of the 7054 Å feature, derived effective temperature, and observed V-band magnitude of Betelgeuse. The methods used to calculate W_λ and T_{eff} are described in §2.3 and §2.5, respectively. For each epoch, Betelgeuse's V-band magnitude M_V and corresponding uncertainty is derived by averaging over the available AAVSO data in bins of ten days each. These results correspond to those presented in Figure 3.3	40
3.2 Predicted and observed change in V-band magnitude of Betelgeuse before, during, and after the Great Dimming, relative to the fiducial epoch of 2020-04-25. Epoch of observation, temperature difference inferred from the strength of the TiO 7054 Å line(ΔT_{eff}), V-band change predicted by PHOENIX models for the given temperature difference (ΔV_{est}), and actual observed V-band change in Betelgeuse (ΔV_{obs}). Here, $\Delta V \equiv (V_T - V_{T_0})$, $\Delta T_{eff} \equiv (T - T_0)$, and $T_0 \equiv 3678$ K. These results correspond to those presented in Figure 3.4	45

LIST OF FIGURES

	PAGE
1.1 Stellar classifications and extended spectral classes on the Hertzsprung-Russell Diagram. Clusters of stars within similar regions are seen to have similar properties, shown by the axes displaying Absolute Magnitude M_V , Effective Temperature T_{eff} (Kelvin), Spectral Class, and Luminosity (L_\odot). Hertzsprung-Russell Diagram courtesy of Harbaugh (2015).	2
1.2 The Gaia Hertzsprung-Russell Diagram of stars within \sim 5000 ly of the Sun. The Density of stars is represented by the correlating color scale. Gaia BP and RP are broad photometric passbands with wavelength ranges 330 – 680 nm and 640 – 1000 nm respectively. The left-hand side shows an approximate temperature and luminosity scale for main-sequence stars. These data display approximately four million stars within five thousand light-years from the Sun (Babusiaux et al. (2018)).	3
1.3 Star chart of the constellation Orion, containing the location of RSG Betelgeuse (α Orionis). The x and y coordinates correspond to right ascension and declination. Star magnitudes are represented by size, with the largest stars being the most easily visible. <i>Image courtesy of ESO, IAU and Sky and Telescope.</i>	5
1.4 The Orion constellation with a zoom towards Betelgeuse. The final image on the right is one of the sharpest images of Betelgeuse, obtained with the Nasmyth Adaptive Optics System Near-Infrared Imager and Spectrograph (NACO) on ESO’s Very Large Telescope (Kervella et al. (2009)).	6
1.5 The surface of Betelgeuse imaged using the Atacama Large Millimeter/submillimeter Array (ALMA). This is the first time that ALMA has ever observed the surface of a star and this first attempt has resulted in the highest-resolution image of Betelgeuse available. Annotation overlaid on the right display the size comparison between Betelgeuse and the orbits of various objects in the Solar System (O’Gorman et al. (2020)).	8
1.6 Nyeeruna, Kambugudha, and the Yugarilya sisters in the sky as seen from southern Australia. Corresponding constellations are labefigured, as well as Nyeeruna’s right club-wielding hand (Betelgeuse) and the left foot of Kambugudha (Aldebaran). (Leaman & Hamacher (2014))	11

1.7	Herschel's light curve of Betelgeuse from 1836 to 1840. Despite Hershel's limited number of observations, the variability is clearly visible (Lloyd (2020)).....	12
1.8	The combined BAA VSS – AAVSO light curve of Betelgeuse from 1893 to the Great Dimming Event's conclusion in 2020. The points are 10-day bins with single points shown as dots, up to 10 points as open circles, and more than 10 as filled circles. The year is shown is shown at the upper left of each panel, each of which spans ~ 25 years (Lloyd (2020)).	13
1.9	The surface of Betelgeuse before, during, and after the dimming event Montargès et al. (2021). The southern hemisphere of Betelgeuse was vastly dimmer than the northern hemisphere during the Great Dimming Event. This is discussed in depth and fully annotated in Figure 1.10.	15
1.10	VLT/SPHERE–ZIMPOL observations of Betelgeuse before, during, and after the dimming event published by Montargès et al. (2021)). North is up; east is left. Montargès et al. (2021) enhanced the contrast using a power-law scale intensity with an index of 0.65. Observations were captured using the $Cnt - H\alpha$ ZIMPOL filter centred at 644.9 nm. The beam size of ZIMPOL is shown in observation (a) by the white disk.	18
1.11	V-band lightcurve of Betelgeuse during the Great Dimming Event courtesy of AAVSO. Vertical black lines indicate epochs of the presented spectra displayed in Tables 1.3 and 1.2. Note the gap in photometric coverage following our 2020-04-25 observation due to solar conjunction.	21
1.12	Final spectrum for each of the five epochs of observation outlined in Tables 1.3 and 1.2.	24
2.1	Notable spectral features shown on the synthetic PHOENIX SED of a Red Supergiant with $T_{eff} = 3300$ K, courtesy of Husser et al. (2013). Red vertical lines correspond to the bandhead of each TiO absorption feature used in determining the spectral types of RSGs.	28
2.2	The process used to measure W_λ, as detailed in §2.3 and §2.4 Top: F_c and the selected feature, with points used to calculate F_c shown via the red dots. The horizontal width of the grey shaded area corresponds to the measured W_λ . The shaded grey area has the same area as the line strength, shown in green. This process for the entire grid of synthetic PHOENIX spectra used in this thesis are shown in Figures A.1 and A.2). The same procedure was also applied to the data of Betelgeuse.	31

2.3	The spectrum of Betelgeuse obtained on 2020-02-15 with prominent spectral features labeled. Red vertical lines correspond to the temperature sensitive TiO absorption features. The grey shading displays the full wavelength range of the 7054 Å TiO feature. The location of the O_2 telluric feature (i.e., the A-band) is marked by a dotted vertical line.	32
2.4	Top: Spectroscopic observations of Betelgeuse. Middle: Each epoch's 7054 Å TiO band with the dotted line corresponding to F_c . Bottom: The normalized 7054 Å TiO for each epoch, displaying clear variations in strengths. It is worth noting the obvious qualitative difference in the strength of this feature between the epochs taken during Betelgeuse's historic minimum (first three epochs) and those taken after it had regained its normal luminosity (final two epochs).	34
2.5	Relation between T_{eff} and W_λ derived from PHOENIX synthetic spectra.	35
2.6	Sensitivity Function for the V-passband as a function of Wavelength λ from Bessell (1990). Tabulated values for the sensitivity function are shown in Table 2.3.	36
2.7	V-passband photometric convolution of a PHOENIX synthetic SED The dotted blue curve displays sensitivity function shown in Figure 2.6. The red SED displays the recorded weighted passband.	38
2.8	ΔM_V as a function of ΔT_{eff} derived by applying the synthetic photometry methods detailed in §2.6. The motivation for choosing $T_0 \equiv 3678$ K is elaborated on in §3.1.	39
3.1	Observed and theoretical spectra. The black spectra displays the normalized 7054 Å TiO feature for each epoch. The red spectrum shows the normalized 7054 Å TiO feature corresponding to a synthetic spectra with the same T_{eff} as inferred for each epoch. The red spectrum is derived from synthetic PHOENIX models via a weighted arithmetic mean. It should be noted that the resolution of the model spectra is much finer than the resolution of the spectra observed for Betelgeuse. This causes the synthetic spectra to display many more dips and rises than the observed spectra.	41

3.2	Top: The Mean V-band Magnitude for each epoch, shown in red, compared to the photometric V-band lightcurve observed during the Great Dimming event. Middle: Each epoch's measured W_λ . Bottom: Inferred values of Betelgeuse's T_{eff} for each epoch, derived from the TiO 7054 Å W_λ relation (§2.5). Values of W_λ and T_{eff} are derived from spectra obtained on 2020-01-03, 2020-01-25, 2020-02-15, 2020-04-25, and 2021-01-09. Calculating uncertainties for W_λ and T_{eff} is described in §3.1.	42
3.3	The W_λ of Betelgeuse's 7054 Å TiO absorption feature, shown in red, fit to the relation between the W_λ of the 7054 Å TiO absorption band and T_{eff} derived in §2.5 from synthetic PHOENIX model spectra.	43
3.4	Values of ΔV_{est} inferred from Betelgeuse's ΔT_{eff} , shown in red, fit to ΔV as a function of ΔT_{eff} derived in §2.6 from synthetic PHOENIX model spectra.	45
3.5	Top: Inferred values of Betelgeuse's ΔT_{eff} . Bottom: Changes in Betelgeuse's V-band magnitude ΔV_{est} (shown in blue) derived from the inferred values of ΔT_{eff} . Observed changes in Betelgeuse's V-band magnitude ΔV_{obs} (shown in red) are included for comparison.	46
A.1	Continuum estimates of the 7054 Å TiO band in all selected PHOENIX synthetic spectra, ranging from 3300 – 4000 Kelvin.	59
A.2	Normalized continuum profiles for the 7054 Å TiO band in all selected PHOENIX synthetic spectra, ranging from 3300 – 4000 Kelvin. The horizontal width of the grey shaded area corresponds to the measured W_λ . The shaded grey area has the same area as the line strength, shown in green.	60

ACKNOWLEDGMENTS

To my parents, thank you for your constant support while I pursue my passions. I could not have done this without you. I would also like to thank my siblings Catherine, Michael and Brian. Catherine, the past few years have included many obstacles. However, I am immensely thankful I had the opportunity to spend most of my masters journey with you by my side. I love you, and I am so proud of you.

Para Denise, te agradezco mucho que me ayudes en mi viaje. Te amo mas que todas las estrellas en el cielo.

I would thank my advisor Dr. Douglas C. Leonard for the instrumental role he has played throughout this thesis. Not only was he the one who introduced this project to me, but his constant guidance and patience has resulted in me becoming a much more confident and passionate astronomer. For this, I am sincerely grateful.

I would like to thank Raymond Remigio for his countless hours of work with Dr. Leonard fixing the 1-m Cassegrain spectrograph that allowed us to obtain the data necessary for this project. Furthermore, I would also like to thank Beatriz Abreau for the help she provided while observing. I would also like to acknowledge Carolyn Heffner and Paul Etzel for their guidance on the use of the spectrograph.

Furthermore, I would like to thank Dr. Robert Quimby and Angela Farrow for their assistance during our observing runs at Mount Laguna Observatory.

Thank you to Dr. Eric Sandquist and Dr. Fridolin Weber for taking the time to serve on my thesis committee.

Finally, to all the friends and family too numerous to name, I am so blessed to be surrounded by countless people supporting my endeavors to become a professional stargazer. To you all, I am eternally grateful.

CHAPTER 1

Introduction

Decoding the light emitted from stars is the primary method used to understand the cosmos. Ancient observers around the globe meticulously catalogued the constellations. Sunlight reflecting off of the planets led to their discovery, as well as the realization that Earth is not the center of the solar system. Though the understanding of the night sky has since increased drastically, the primary source of information for astronomers is still visible light. However, stars come in a large range of masses, ages, and compositions, each with unique properties.

Stars are organized by temperature using the Harvard spectral classification sequence. Annie Jump Cannon organized stars into spectral types O-B-A-F-G-K-M. This sequence arranges stars based on their temperatures, with O stars being the hottest stars, and M being the coolest (Carroll & Ostlie (2006)). Each spectral type is further divided into subclasses ranging from 0 – 9, with 0 representing the hottest stars and 9 representing the coolest stars. Stars can also be described by their luminosity class. Luminosity Classes are determined from the unique spectral features identified in a star's spectral energy distribution (SED), which is a visualization of the energy emitted by the star as a function of its frequency or wavelength (LeBlanc (2010)).

The Hertzsprung-Russell (H-R) Diagram is a powerful tool used by astronomers to visualize the relationship between the luminosity (or absolute magnitude) and color index, stellar classification, or effective temperature (T_{eff}) for a population of stars in various evolutionary phases. Figure 1.1 illustrates that stars are not randomly scattered on the H-R diagram. The distinctive curve that stretches across the H-R diagram from the top left to the bottom right is the main sequence (MS). The main sequence is populated by stars that are steadily fusing Hydrogen in their cores. Modern calculations estimate that $\sim 90\%$ of stars lie on the main sequence (Babusiaux et al. (2018)). O and B stars occupy the top left of the main sequence. These are the hottest and most massive main sequence stars. The most numerous stars, K and M stars, populate the bottom right of the H-R diagram.

A grand majority stars begin their lives on the main sequence as low mass stars, with K and M stars being the most common. M stars alone account for $\sim 75\%$ of main sequence stars (Ledrew (2001)). Although much can be learned through studying low mass stars, high-mass stars are a critical component for many different disciplines of

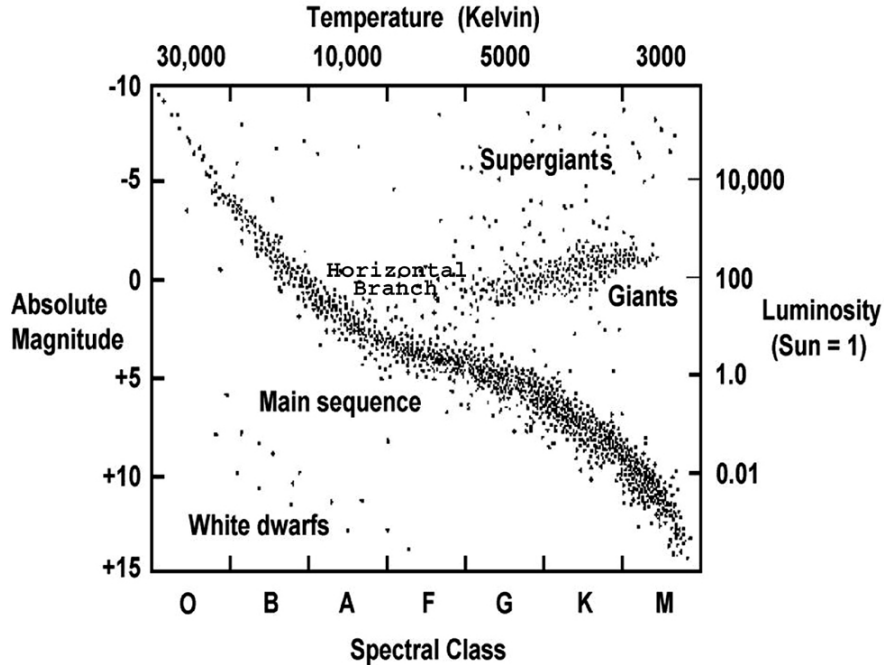


Figure 1.1. Stellar classifications and extended spectral classes on the Hertzsprung-Russell Diagram. Clusters of stars within similar regions are seen to have similar properties, shown by the axes displaying Absolute Magnitude M_V , Effective Temperature T_{eff} (Kelvin), Spectral Class, and Luminosity (L_\odot). Hertzsprung-Russell Diagram courtesy of Harbaugh (2015).

astronomy. While high-mass stars are young, astronomers use them as clear indicators of star forming regions, as they easily outshine neighboring low mass stars. The H-R diagram from Gaia Data Release Two, shown in Figure 1.2, clearly shows that low mass stars greatly outnumber high mass stars. Post-MS giant stars are even rarer. Though populations of both extragalactic and milky way high-mass stars have been studied in detail, the physical properties of their evolution are still poorly constrained (Babusiaux et al. (2018)).

Stars on the H-R diagram are not distributed randomly. Stars populating each distinct population share many common features and properties. Stars no longer on the main sequence can be seen clustering together in clear distinct groups on the H-R diagram, displayed in Figure 1.1. Depletion of Hydrogen in the core of the star marks the end of its main sequence lifetime. The lack of Hydrogen to fuse in the core of a star disrupts the fine balance between internal and external pressure. This balance, known as hydrostatic equilibrium, is supported by outward pressure fueled by Hydrogen fusion counteracting inward gravitational forces resulting from the mass of the star. The initial mass of an individual star determines exactly how it transitions off the main sequence. High-mass post-MS stars actively fusing heavier atomic nuclei are classified

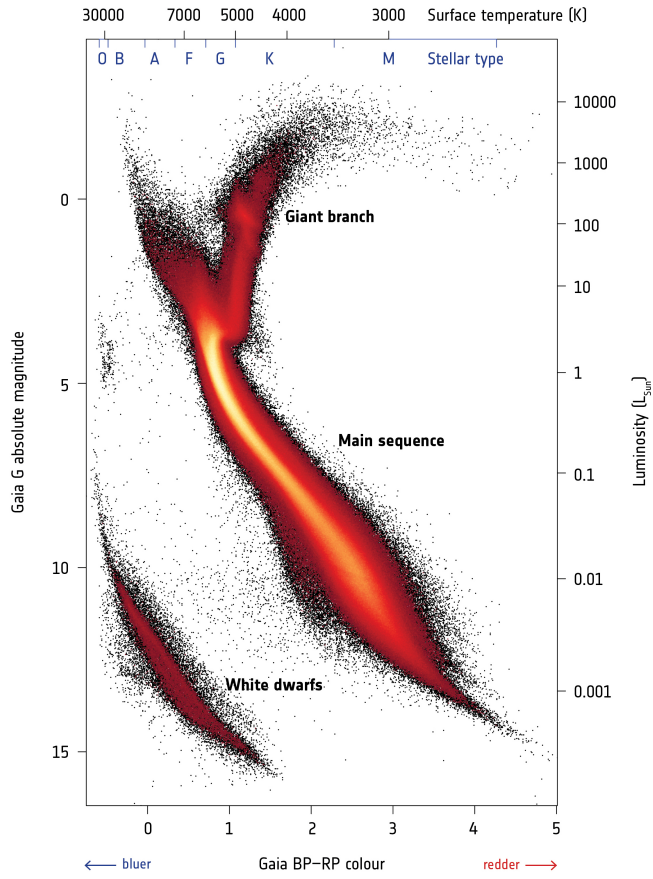


Figure 1.2. The Gaia Hertzsprung-Russell Diagram of stars within ~ 5000 ly of the Sun. The Density of stars is represented by the correlating color scale. Gaia BP and RP are broad photometric passbands with wavelength ranges $330 - 680$ nm and $640 - 1000$ nm respectively. The left-hand side shows an approximate temperature and luminosity scale for main-sequence stars. These data display approximately four million stars within five thousand light-years from the Sun (Babusiaux et al. (2018)).

as supergiant stars (Carroll & Ostlie (2006)). The end of a high-mass star's lifetime is triggered during an explosive death known as a supernova. Supernovae offer valuable glimpses into the chemical enrichment of galaxies. However, high-mass stars are rare. The progenitor stars for type-II supernovae, stars with initial masses greater than $8 M_{\odot}$, account for less than 0.1% of all main sequence stars (Levesque (2017)). White dwarfs are the final stage of stellar evolution predicted for stars smaller than $\sim 8 - 10 M_{\odot}$. However, accreting white dwarfs may be the progenitor for type Ia supernovae (Carroll & Ostlie (2006)). Red Supergiants (RSGs) are evolved Helium-burning post-MS stars

with initial masses $\gtrsim 8M_{\odot}$. Stellar Evolution models predict that these stars represent a vital step in a galaxy's chemical evolution (Kiss et al. (2006)).

1.1 Variability in Red Supergiants

RSGs often display some degree of visual variability, which is common for stars such as these which are in the process of transitioning off of the main sequence.

Variable stars are defined as stars exhibiting temporal changes, both regular and irregular. These changes can be either photometric, spectroscopic, or both. (Goldberg (1984); Stothers (1969, 2010)). Variable stars can be divided into subcategories based on their pulsation behavior. Variable RSGs are most often classified in one of the following classes: rotating, eruptive, explosive, and pulsating stars.

The mechanism for variability in rotating variables is not due to an intrinsic and internal property of the star. Instead, variability is caused by activity on the surface or some other externally related phenomena. For example, events such as starspots, tidal disruptions from a companion star, and eclipsing binaries can all cause a star to appear variable. These would all be classified as rotating variables. Conversely, eruptive, explosive, and pulsating variables all display variability intrinsic to the individual star (Carroll & Ostlie (2006)). Mass loss events are commonly observed in RSGs, and stars such as these with non-periodic mass ejection events are often classified as eruptive variables. Explosive variable stars are classified by their semi-periodic mass ejection events. The most dramatic example of an explosive variable is a supernovae.

Pulsating variables display both photometric and spectroscopic variations. The variation is often periodic and driven by changes in stellar radius, T_{eff} , or a combination of both. Pulsating variables can be further sub-categorized. Variable stars with periods ranging from 30 – 100 days are classified as long-period variables (LPVs) (LeBlanc (2010)). Cepheid Variables are one example. Cepheid variable stars are high-mass stars ($\gtrsim 8 M_{\odot}$) that expand and contract in a repeating and predictable cycle. These stars are excellent distance indicators, since there is a strong relationship between their period of variation and intrinsic luminosity (Leavitt & Pickering (1912)).

There are two subclasses of LPVs: Mira and Semi-regular, each classified by their pulsation behavior. Mira variables are pulsating red giants evolving through the red giant branch typically displaying variation periods of $\sim 80 - 1000$ days. The photometric light curves of Mira variables show regular, oscillatory periods that can vary by 2.5 magnitudes.

Semi-regular variables are moderately unstable M-giants and supergiants with a large mass range of $\sim 1 - 30M_{\odot}$. These stars display significant periodicity in light

changes, with many semi-regular variables exhibiting two prominent periods, a primary and secondary (P_1 and P_2 , respectively), which results in an irregular photometric light curve that can vary by ~ 2.5 mag (Kiss et al. (2006)). Variations in P_1 typically last $\sim 30 - 500$ days. Secondary variations correlated with P_2 can be either semi-regular or irregular (van Altena et al. (1995); Stothers (2010)). Betelgeuse, a bright RSG in the constellation Orion, is a famous semi-regular variable (Levesque (2017)). §1.2.2 discusses Betelgeuse's variability in further detail.

1.2 Betelgeuse

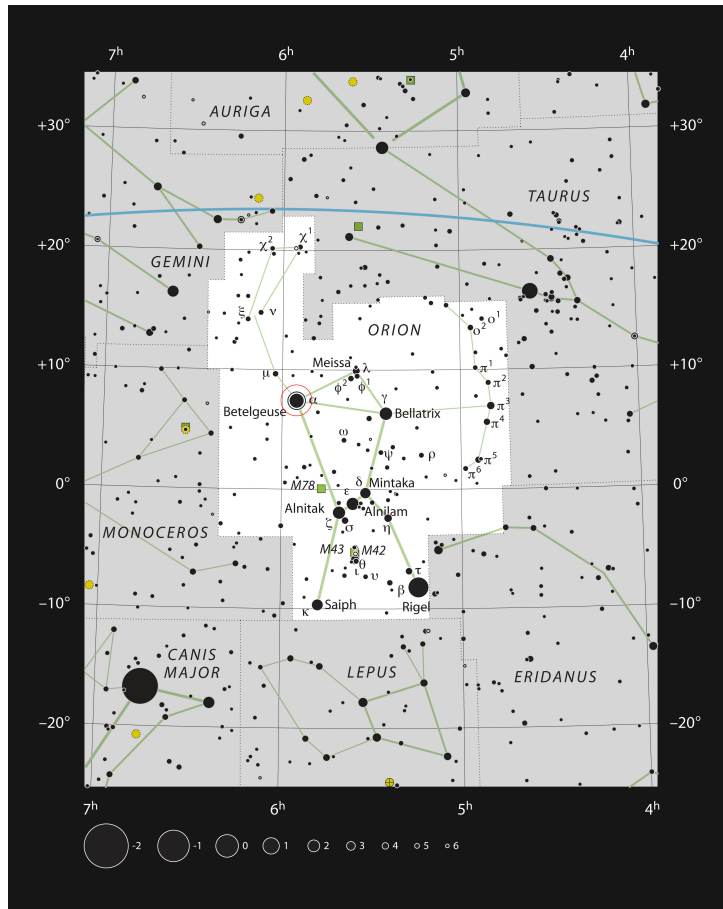


Figure 1.3. Star chart of the constellation Orion, containing the location of RSG Betelgeuse (α Orionis). The x and y coordinates correspond to right ascension and declination. Star magnitudes are represented by size, with the largest stars being the most easily visible. *Image courtesy of ESO, IAU and Sky and Telescope.*

Betelgeuse is one of the most recognizable stars in the night sky. A star chart of the constellation Orion displaying the location of Betelgeuse is shown in Figure 1.3.

The crimson star adorning Orion’s shoulder is easily visible with the naked eye. Orion viewed from the northern hemisphere is shown in Figure 1.4. Betelgeuse is the closest RSG. As a result of its proximity and large angular diameter the star is incredibly luminous. These combined characteristics make Betelgeuse an ideal candidate for RSG studies. However, parameters such as its distance, diameter, and temperature are still poorly constrained (Kravchenko et al. (2021)). Accurately modeling RSG evolution is a critical component for many different disciplines of astronomy, yet this class of stars prove difficult to study.



Figure 1.4. The Orion constellation with a zoom towards Betelgeuse. The final image on the right is one of the sharpest images of Betelgeuse, obtained with the Nasmyth Adaptive Optics System Near-Infrared Imager and Spectrograph (NACO) on ESO’s Very Large Telescope (Kervella et al. (2009)).

Starting in late 2019, Betelgeuse provided clear evidence that RSGs are not completely understood. Usually one of the brightest stars in the sky, it started to become drastically dimmer in October 2019. At its dimmest, Betelgeuse dropped from being the 10th brightest star in the sky to not even being one of the brightest 20 (Levesque & Massey (2020)). This event, spanning October 2019 to March 2020, is deepest minimum in brightness recorded for Betelgeuse (Guinan et al. (2020)). While Betelgeuse typically varies in brightness, this dimming event drastically conflicted with predictions. While Betelgeuse’s dimming event did not mark the end of the giant’s life as popular media had speculated and hoped, eg. Mack (2020), it was a clear reminder of the uncertainties still prevalent in one of the most studied stars. Multiple explanations have been provided for this surprise dimming. A decrease in the surface temperature of the star would cause Betelgeuse to dim. The decline in surface

temperature may be localized to one or more spots, potentially caused by massive convective cells bringing large portions of cooler material to the star's surface (Harper et al. (2020); Alexeeva et al. (2021); Dharmawardena et al. (2020)). Light from the star may also be extinguished by newly formed dust ejected from Betelgeuse during a mass loss event (Montargès et al. (2021); Dupree et al. (2020)). A transiting dust cloud in the line of sight of Betelgeuse may also be the cause of this unexplained dimming episode (Levesque & Massey (2020)).

Betelgeuse's unpredictable behavior, brightness, and proximity make it an optimal target for the study of RSG evolution. If Betelgeuse's parameters can be accurately constrained, it will prove invaluable not only for stellar evolutionary theory, but for the astronomy community as a whole.

1.2.1 Physical Characteristics

Betelgeuse is a SRc variable RSG. SRc variables are a subclass of semi-regular variables containing supergiant stars. The star is an early M-Type supergiant with an M1-2Ia-ab spectral type, resulting in the surface's famous orange color as the cooler late M-type supergiants, for example most Mira variables, display a deeper red surface color. (Lloyd (2020); Keenan & McNeil (1989)). Typically the tenth brightest star in the sky, Betelgeuse is massive, nearby, and incredibly bright. Stellar evolutionary models estimate that the RSG is $\sim 8.0 - 8.5$ Myr old, suggesting the star will supernova in less than 100,000 years as a Type II-Plateau (Type-IIP) Supernova (Dolan et al. (2016)). Typically these are ideal qualities for an observation target. However, Betelgeuse's uncertainty in proper motion, variability, asymmetry, and large angular diameter present astronomers with many challenges. Over the years, Betelgeuse has been an object of interest for astronomers, and thus, a great deal of data have been amassed for the star. The century-long lightcurve shown in Figure 1.8 clearly illustrates the consistent interest surrounding Betelgeuse. Despite the data available, the accuracy and precision of this data vary dramatically. Thus, it is crucial to understand the analysis, observations, and modeling responsible for the specific parameters adopted in Betelgeuse studies. The following section will explore the history, methods, and measurements of Betelgeuse's physical parameters.

Betelgeuse has the largest apparent size of any star in the night sky. Betelgeuse's surface is resolvable, due to its proximity and extended radius. ALMA observations of the surface of Betelgeuse illustrating the star's immense volume are shown in Figure 1.5. Angular diameter derivations for Betelgeuse are complicated by various factors inherent to RSGs. RSGs are extended in radius, causing their surface

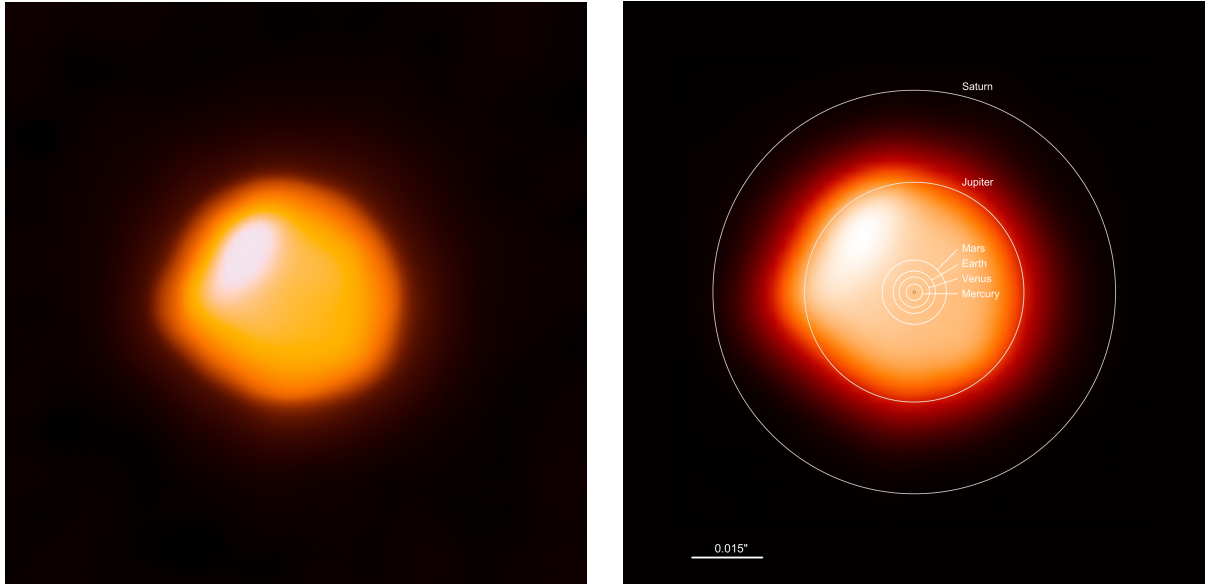


Figure 1.5. The surface of Betelgeuse imaged using the Atacama Large Millimeter/submillimeter Array (ALMA). This is the first time that ALMA has ever observed the surface of a star and this first attempt has resulted in the highest-resolution image of Betelgeuse available. Annotation overlaid on the right display the size comparison between Betelgeuse and the orbits of various objects in the Solar System (O’Gorman et al. (2020)).

gravity to be much lower than a main sequence star. As a result, Betelgeuse’s extended atmosphere and deep convective motion produces an asymmetrical shape as well as random variability in surface luminosity and temperature. This random variability is also paired with multiple, separate, periodic fluctuations in luminosity and temperature (Levesque (2017)). Furthermore, the optical depth of Betelgeuse is wavelength dependant, meaning measurements made at one wavelength yield a different angular diameter than measurements made at another. Published angular diameters are typically distributed into two distinct wavelength groups. The first, $\lambda \approx 1 \mu m$ yields angular diameters with a median around $\theta \approx 44$ mas. The second group of results $\lambda \approx 10 \mu m$ yields angular diameters focused around $\theta \approx 57$ mas (Dolan et al. (2016)).

Further, the angular diameter must also be corrected for the effects of limb darkening. Limb darkening is an optical effect which causes the central parts of the star to appear brighter than the edges to an observer. Since the temperature increases with depth in the atmospheres of stars, an observer sees the deepest, warmest, and therefore brighter layers of the star at the center of the star, while at the edges of the star cooler and dimmer layers are visible (Carroll & Ostlie (2006)). The inferred disk for effects of limb darkening tends to diminish the observed radius relative to the

Rosseland mean radius. This correction can be as much as 10% in visible wavelengths or as little as 1% in the near infrared (Weiner et al. (2003)).

Historically, Betelgeuse's large angular diameter has been a significant obstacle when attempting to derive an accurate parallax, thus making the determination of the distance to this star difficult. Since Betelgeuse's angular size is considerably larger than the star's parallax, a well-constrained angular diameter is a crucial parameter for the astrometric solutions necessary to account for the star's large apparent size. Furthermore, the angular diameter of Betelgeuse changes drastically over time, further complicating distance measurements (Townes et al. (2009); Harper et al. (2008)).

The outcome of the obstacle relating to Betelgeuse's angular diameter is varying and conflicting conclusions of Betelgeuse's parallax and distance. Hipparcos, a satellite launched by the European Space Agency (ESA) in 1989, greatly improved the capabilities of measuring the parallaxes of stars, thus leading to better distances. Prior to Hipparcos, the best measured parallax of Betelgeuse came from the Yale Trigonometric Parallax Data Catalog (van Altena et al. (1995)).

Hipparcos measured a parallax for Betelgeuse of $\pi \approx 7.63 \pm 1.64$ mas, yielding a distance of 131 ± 30 pc (Perryman et al. (1997)). Due to the observational difficulties associated with Betelgeuse, the original Hipparcos parallax had significant uncertainties. In 2007, the Hipparcos parallax was revised to $\pi \approx 6.56 \pm 0.83$ mas (van Leeuwen (2007)). However, a year later, Very Large Array (VLA) radio positions of Betelgeuse were combined with the revised Hipparcos Catalogue Astrometric Data to derive a new parallax. From this combined data, the derived parallax and distance were 5.07 ± 1.10 and 197 ± 45 pc, respectively (Harper et al. (2008)). Nearly a decade later, the position of Betelgeuse was revisited by combining Hipparcos parallax data with existing data from multiple radio observatories (VLA, e-MERLIN and ALMA), yielding a parallax of $\pi \approx 4.51 \pm 0.080$ mas and a distance of 222^{+48}_{-34} pc (Harper et al. (2017)). In June 2020, new distance estimates for Betelgeuse were derived by combining the 2017 parallax measurement with results from three different modeling techniques. This resulted in a parallax and distance of $\pi \approx 6.06^{+0.31}_{-0.52}$ mas and 165^{+16}_{-18} pc, respectively (Joyce et al. (2020)). However, these measurements are recent and based on modeling data. The 2017 parallax is currently the most common measurement of Betelgeuse's parallax and distance cited for modern Betelgeuse studies.

Because Betelgeuse is a star with no companion, there is not a direct method of measuring the present day mass of the star. One estimate combines limb darkening laws, models of stellar atmospheres, and interferometric observations to calculate a present day mass of $11.6^{+5.0}_{-3.9} M_{\odot}$ (Neilson et al. (2011)). However, a more recent

estimation provided by Joyce et al. (2020) combines MESA evolutionary, asteroseismic, and hydrodynamical simulations with new photometric data, suggesting a present day mass range of $16.5 - 19 \text{ M}_\odot$.

RSGs shed a significant amount of mass over the course of their lifetime. Therefore, when discussing the mass of a RSG such as Betelgeuse, it is most convenient to consider the progenitor mass. A combination of stellar evolutionary models calculate that Betelgeuse is most likely descended from a main sequence star with an initial mass of $\sim 20^{+5}_{-3} \text{ M}_\odot$ (Meynet et al. (2013); Dolan et al. (2016)). For a star such as Betelgeuse, more than half of the mass loss that occurs in the star's lifetime happens post main sequence. Most of this post main sequence mass loss occurs during the RSG phase, when the surface gravity is at its lowest (Levesque (2017)). A combination of models and observations have confirmed that the mass ejection and motion of Betelgeuse have created a bow shock in the direction of motion. However, multiple bow shocks of varying sizes have also been confirmed suggesting that Betelgeuse loses mass episodically rather than continuously (Dolan et al. (2016)).

Similar to the derivations for Betelgeuse's angular diameter, calculations of the radii must be corrected for limb darkening and wavelength. These corrections are the smallest for the $11 \mu\text{m}$ measurements (Weiner et al. (2003)). Though the radius varies periodically, most stellar evolutionary models of Betelgeuse adopt a radius of $887 \pm 203 \text{ R}_\odot$ (Dolan et al. (2016)).

Due to the previously mentioned difficulties in measuring an accurate distance for Betelgeuse, as well as the star's inherent variability, it is difficult to assign a mean value for the star's temperature and luminosity. Modern estimates of Betelgeuse's surface temperature have significant uncertainties, and individual measurements can vary by nearly 200 K. (Levesque & Massey (2020)). The temperature of Betelgeuse is typically calculated using the titanium oxide (TiO) absorption bands commonly used to identify stars of this spectral type. This is discussed in further detail in Chapter 2.

Parameter	Value	References
\log_g (cm/s^2)	0.08	(Josselin & Plez (2007))
Initial Mass (M_\odot)	$18 - 21$	(Joyce et al. (2020))
Radius (R_\odot)	1021	(Ohnaka et al. (2011))
$\log(\text{L}/\text{L}_\odot)$	5.10 ± 0.22	(Harper et al. (2008))
Mass loss ($\text{M}_\odot \text{ yr}^{-1}$)	1.2×10^{-6}	(Bertre et al. (2012))

Table 1.1. Atmospheric and Surface parameters for Betelgeuse.

1.2.2 Variability

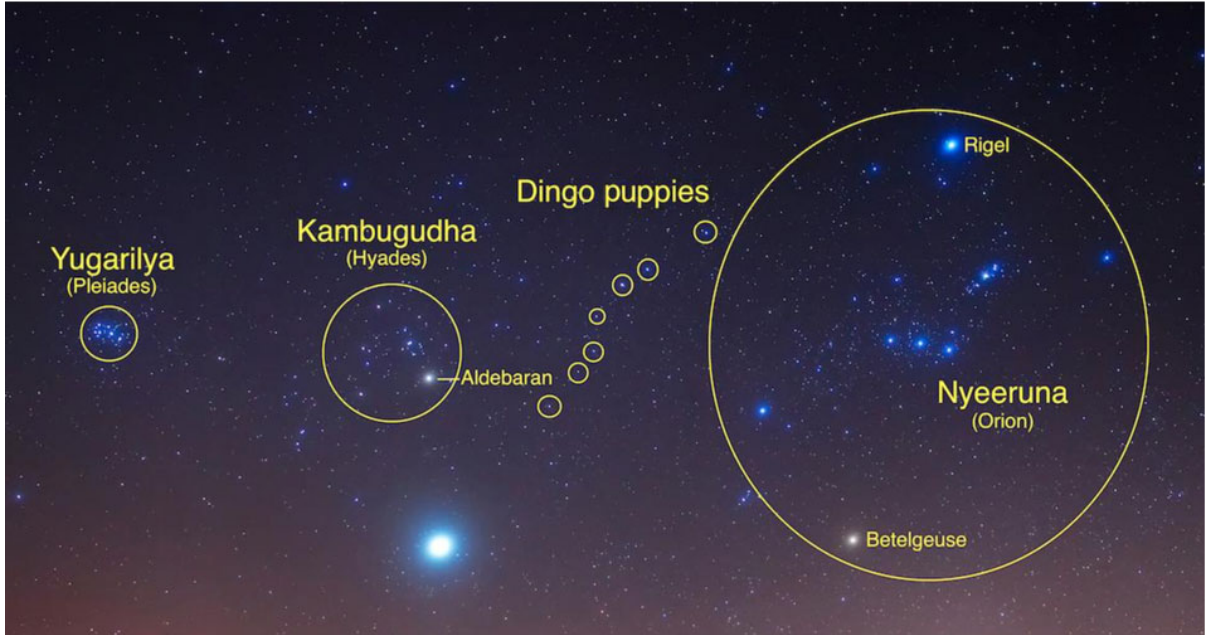


Figure 1.6. Nyeeruna, Kambugudha, and the Yugarilya sisters in the sky as seen from southern Australia. Corresponding constellations are labefigureled, as well as Nyeeruna's right club-wielding hand (Betelgeuse) and the left foot of Kambugudha (Aldebaran). (Leaman & Hamacher (2014))

Betelgeuse's classification as a variable star is not a modern discovery. As a bright star located in a prominent constellation, the changes in brightness can be easily noticed with the naked eye and a consistent and dedicated observer (Schaefer (2018)). Ancient astronomers worldwide noticed the unique properties of Betelgeuse. While references of variable stars appear in the mythologies of many ancient cultures, Aboriginal Australian oral tradition potentially contains the first direct description of Betelgeuse's variability. In the oral tradition, a skilled hunter named Nyeeruna comprises the stars of Orion. Betelgeuse is the club carrying right hand of Nyeeruna. Nyeeruna is a vain womanizer set on pursuing the Yugarilya sisters, commonly known as the Pleiades. The eldest sister Kambugudha, corresponding to the constellation Hyades, is protective of her younger siblings. She refuses to let Nyeeruna near the Yugarilya sisters. An angry Nyeeruna fills his right hand (Betelgeuse) with 'fire magic', but Kambugudha defends her sisters by filling her foot, Aldebaran, with her own fire magic. The narrative explicitly states that the right club-wielding hand of Nyeeruna (Betelgeuse) brightens with fire magic/lust, then fades before fading again over time. The left foot of Kambugudha (Aldebaran) is also clearly mentioned increasing in

brightness before fading over time, but with the amazing note of having less frequent and less intense changes in brightness. Nyeeruna (Orion), Kambugudha (Hyades), and the Yugarilya sisters (Pleiades) observed from Southern Australia are shown in Figure 1.6 (Hamacher (2018)).

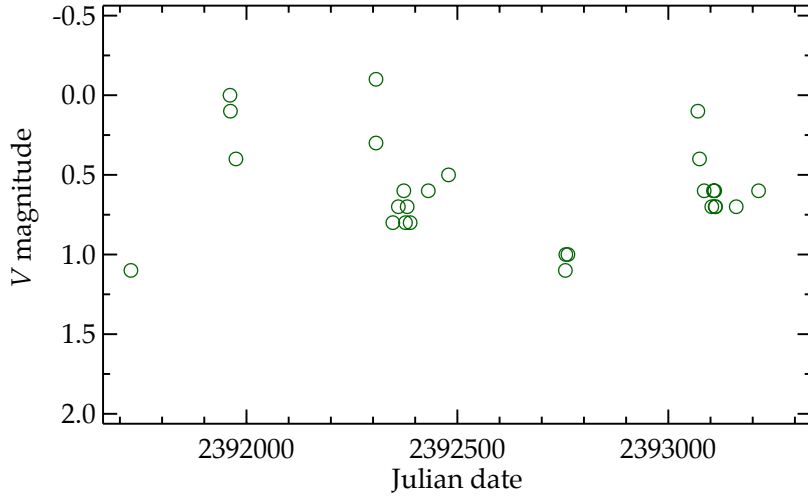


Figure 1.7. Herschel's light curve of Betelgeuse from 1836 to 1840. Despite Hershel's limited number of observations, the variability is clearly visible (Lloyd (2020)).

Betelgeuse's variability was formally rediscovered by Sir John Herschel in 1839. Herschel's observations were dedicated to creating an “*Order of Lustre*” with the goal of creating a sequence of stars arranged by brightness. After three years of observations, he was surprised to find that Betelgeuse’s rank in the sequence was not consistent. Herschel was further shocked that Betelgeuse varied in brightness by ~ 1.1 mag in the V-band. His observations of Betelgeuse are shown in Figure 1.7. He reported his findings in 1840. However, only a handful of astronomers in the community noticed his findings and joined the new field of variable star astronomy. Luckily, Betelgeuse’s brightness made it an easy target for variable star organizations. Today, the most notable of these organizations include The British Astronomical Association Variable Star Section (BAA VSS) and The American Association of Variable Star Observers (AAVSO), whose combined lightcurve is shown in Figure 1.8 (Lloyd (2020)).

While Betelgeuse is variable on multiple timescales, the two periods of $P_1 \approx 430$ day and $P_2 \approx 5.8$ yr stand out as the clear primary and secondary timescales of variation (Levesque & Massey (2020); Kiss et al. (2006); Stothers (2010)). Both periods

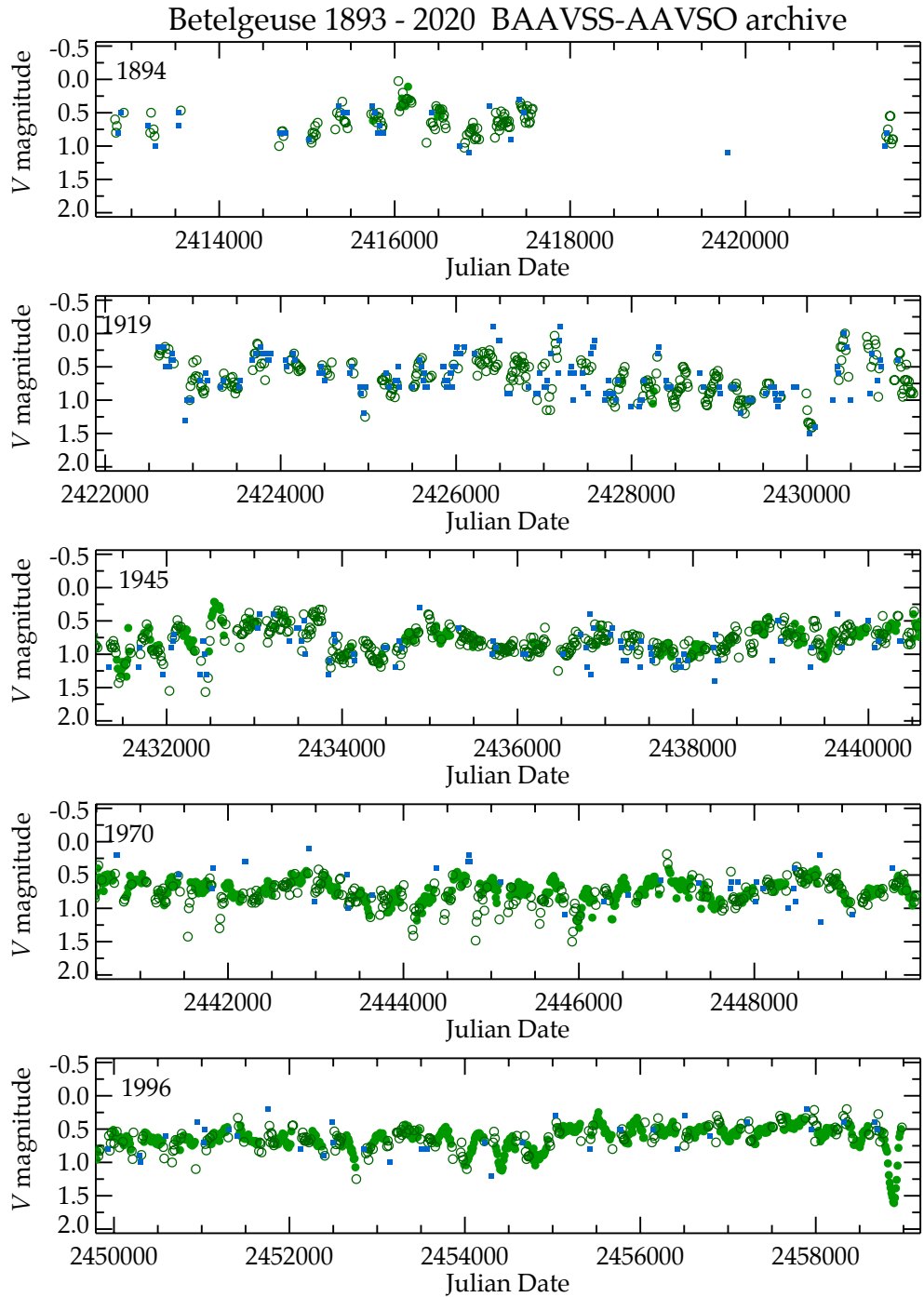


Figure 1.8. The combined BAA VSS – AAVSO light curve of Betelgeuse from 1893 to the Great Dimming Event’s conclusion in 2020. The points are 10-day bins with single points shown as dots, up to 10 points as open circles, and more than 10 as filled circles. The year is shown at the upper left of each panel, each of which spans ~ 25 years (Lloyd (2020)).

are semi-regular in nature, with separate proposed physical mechanisms behind each variation in brightness. Deep convective activity as well as opacity and ionization mechanisms inherent to some RSG cause the radius of these stars to change drastically and periodically. Betelgeuse's primary period is believed to be a result of radial pulsations driven by the κ -mechanism, which occurs when the opacity (κ) of a star increases with temperature. Inward motion of a star's atmosphere compresses material in the upper layers, increasing the density and opacity. More radiation is trapped as the opacity increases. The accumulation of heat and pressure eventually pushes these layers back outward. This causes the star to display a cyclical process of expansion and contraction. As the outer layers of the star expand and shrink, the temperature rises and falls, which causes the brightness of the star to act in kind (Stothers (1972)).

The origin of the very long secondary period is still a mystery and it's very existence remains somewhat contested in the community (Lloyd (2020)). Betelgeuse's secondary period (~ 2100 days) cannot be explained by radial pulsations, as the timescale for the secondary period is much longer than the radial pulsation period of RSGs. Longer pulsation timescales can only be achieved with unrealistically low temperatures, uncharacteristically high luminosities, or very high initial stellar masses (Stothers (2010)). The best matching suggestion to observations is still that of Schwarzschild (1975) which posits that the secondary period may be reminiscent of the fact that RSGs have a few, massive granulation cells with sizes comparable to the stellar radius. These massive cells cause the brightness of the star to fluctuate independently from the variation caused by radial pulsations (Levesque (2017)).

1.3 Dimming Episode

Starting in November of 2019, Betelgeuse's brightness started rapidly decreasing. Reports of the dimming event by Guinan et al. (2019) rekindled interest in Betelgeuse, resulting in an avalanche of new observations of the variable star. Variability in the brightness of this star is expected, however this fading was unusually deep and rapid. The presence of two clear patterns in brightness (along with many other random variations) assumes that the brightness of Betelgeuse will have peaks and dips in brightness as P_1 and P_2 align constructively and destructively. Multiple studies, namely Harper et al. (2020), Guinan et al. (2020), and Sigismondi (2020), have noted that the dominant period ($P_1 \approx 430$ day) and its long-period ($P_2 \approx 5.8$ yr) coincided in February 2020, when Betelgeuse's V-band magnitude was at its dimmest. However, the observed decline in luminosity cannot be explained by the coinciding periods alone.

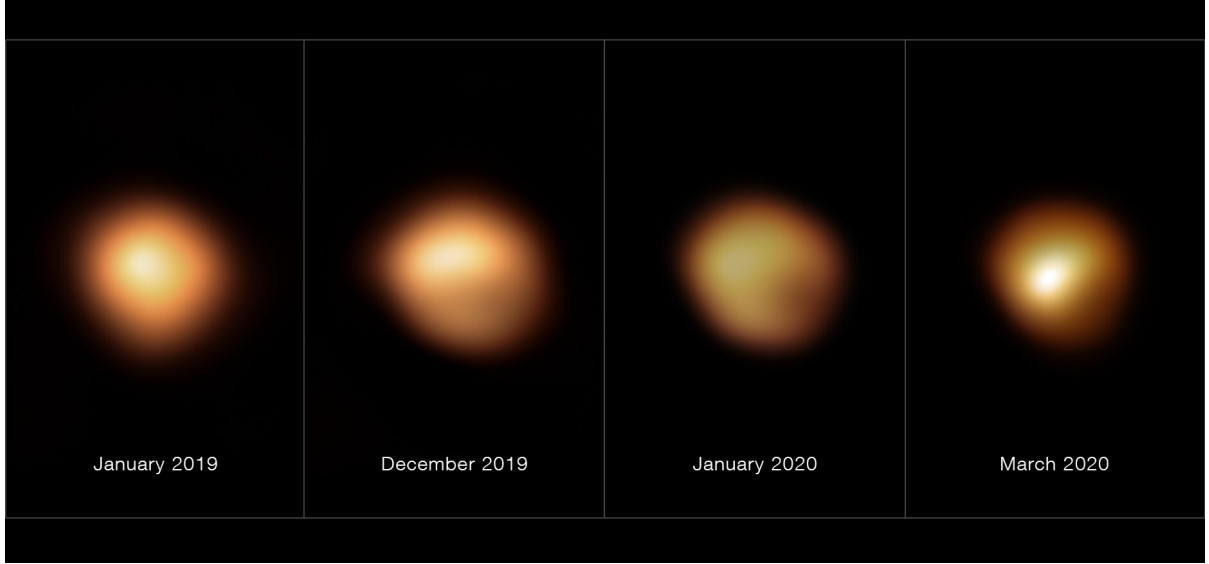


Figure 1.9. The surface of Betelgeuse before, during, and after the dimming event Montargès et al. (2021). The southern hemisphere of Betelgeuse was vastly dimmer than the northern hemisphere during the Great Dimming Event. This is discussed in depth and fully annotated in Figure 1.10.

Betelgeuse most often has an apparent magnitude between $\sim 0.1 - 1.0$ mag. However, by February of 2020, Betelgeuse's visual and V-band magnitude plummeted. February's V-band magnitude of 1.6 mag is the deepest minimum in brightness recorded, clearly visible in the context of a century of variation available in Figure 1.8. Furthermore, high angular resolution observations revealed that Betelgeuse was not uniformly bright throughout the event as a large spot was visible on the southern hemisphere. In fact; the southern hemisphere is estimated to have been about ten times darker than usual (Montargès et al. (2021)). These observations are introduced by Figure 1.9. After this event, at which Betelgeuse reached a minimum of only 35% its usual brightness, the star's brightness rapidly increased over the next few months. Both professional and amateur astronomers worldwide were captivated by the challenge Betelgeuse presented. Nearly two years later, many potential scenarios have been put forward to explain this mysterious phenomenon, including:

1. Betelgeuse is showing early signs of a pre-phase supernova (George et al. (2020))
2. Strong stellar winds causing fluctuations in the observed color and brightness of Betelgeuse (Davies & Plez (2021))
3. Betelgeuse's radius decreasing due to a change in the star's photosphere (Dharmawardena et al. (2020))

4. A cloud of dust not produced by Betelgeuse passing between the star and our line of sight (Levesque & Massey (2020))
5. An occultation of newly formed dust as a result of a mass loss extinguishing light from the star (Dupree et al. (2020); Montargès et al. (2021))
6. A drop in Betelgeuse's T_{eff} , localized to a cool patch in the photosphere (potentially linked to a mass loss event) (Harper et al. (2020); Alexeeva et al. (2021); Kravchenko et al. (2021))

We now discuss each of these scenarios, in turn.

1.3.1 Pre-Phase Supernova

The unexpected decline in brightness observed during the dimming event led to some speculation that Betelgeuse was preparing to go supernova. Betelgeuse is a high-mass star towards the end of its lifetime. Studies have theorized that supernovae for RSGs such as Betelgeuse may be preceded by variations in the light curve that drastically differ from the star's long term light curve as a result of eruptive mass loss events prior to explosion (Fuller (2017)). However, while these drastic variations have been observed in the weeks to months leading up to other types of supernovae, this behavior has not been confirmed in RSGs preceding a Type-IIP supernova (Johnson et al. (2018)).

Some have proposed that the dimming event may be a potential warning sign of a critical change within the dynamical systems of Betelgeuse. George et al. (2020) suggest that this may be the case with Betelgeuse. By analyzing Betelgeuse's lightcurve from the early 1980's through the dimming event, they show that signatures of an impending change in the nonlinear dynamics can be observed in the properties of the lightcurve preceding the dimming episode. From these results, George et al. (2020) concludes that the dimming episode may be an indication of a major change in the pulsation dynamics of the star.

It is unlikely that the dimming event is a result of Betelgeuse's imminent destruction. While some have suggested that core collapse supernovae are preceded by periods of increased mass loss, this is heavily contested (Fuller (2017)). The current mass loss rate of $1.2 \times 10^{-6} M_{\odot} \text{ yr}^{-1}$ (Table 1.1) does not suggest that Betelgeuse has entered the final evolutionary stages preceding a supernovae (Bertre et al. (2012)). However, predicting exactly when a RSG will supernova based on the surface activity is difficult. As RSGs proceed through the final stages of evolution preceding a supernova, the envelope becomes unable to react to changes in the core. It has been shown that supernova caused by instabilities in nuclear burning or shock-waves resulting from

vigorous core convection often do not display variations in brightness larger than $\sim 5 - 10\%$, suggesting that Type-IIP supernovae are not always preceded by drastic variations in brightness (Smith & Arnett (2014); Woosley & Heger (2015); Fuller (2017); Quataert & Shiode (2012)). While it is unlikely that the dimming event is a result of Betelgeuse entering this phase, results cannot completely discount the possibility that a supernova is Betelgeuse's imminent fate, since RSGs can detonate with little to no warning.

1.3.2 Stellar Winds

An analysis by Davies & Plez (2021) provides evidence that synthetic model spectra fail to account for strong stellar winds. They propose that fluctuations in spectral variability seen during Betelgeuse's dimming event can result from variations in RSG winds driven by mass loss by showing that the addition of wind to MARCS model atmospheres can increase the strength of TiO absorption features. Furthermore, they show that a period of increased mass loss can reproduce the increased strength of TiO bands measured during Betelgeuse's dimming episode while maintaining a constant T_{eff} .

1.3.3 Variable Photosphere and Radius

Another proposed phenomena responsible for Betelgeuse's observed decrease in luminosity is a change in the star's photosphere resulting in a decreasing radius. Dharmawardena et al. (2020) reports that Betelgeuse's luminosity decreased by $\sim 20\%$ in the 450 and $850 \mu m$ sub-mm fluxes. Their radiative-transfer modeling show that the observed decrease at these wavelengths cannot be caused by changes in the dust envelope, rather, it must correspond to a change in Betelgeuse's photosphere. Their analysis finds that the change in the photosphere can take one of two forms. If Betelgeuse's T_{eff} remained constant throughout the dimming event, the observed reduction in luminosity is a result of the star's radius decreasing by $\sim 10\%$. However, Dharmawardena et al. (2020) also show that a large localized cool patch in the photosphere can reproduce their observations. The analysis of high resolution spectra of Betelgeuse during the dimming event provided by Alexeeva et al. (2021) estimates Betelgeuse's \log_g by comparing the strength of Ca II lines at 8542 and 8662 \AA to a grid of MARCS models varying in \log_g . They choose these Ca II lines since they are highly sensitive to \log_g while being minimally sensitive to T_{eff} . Alexeeva et al. (2021) concludes from this analysis that Betelgeuse's radius remained constant throughout the dimming event, ruling out pulsation as a possible mechanism.

1.3.4 Dust Occultation

Levesque & Massey (2020) provided an early claim that the drop in V-band magnitude was most likely a result of newly formed dust transiting between Betelgeuse and our line of sight. They compare synthetic model spectra derived from MARCS stellar atmospheres to spectral observations of Betelgeuse during the dimming event as well as spectral observations from 2004. The wavelength range of their spectra is 4000–6700 Å, which includes the temperature sensitive TiO absorption features with bandheads at 4761 Å, 4954 Å, 5167 Å, 5448 Å, 5847 Å, and 6158 Å. By comparing the strength of these bands to their selected grid of synthetic MARCS SEDs, Levesque & Massey (2020) derived an $T_{eff} = 3600 \pm 25$ K while Betelgeuse was at its minimum brightness, which is only 50 K cooler than the T_{eff} inferred from their 2004 observations. From these results, they conclude that the star’s surface temperature was not cool enough to result in the observed dimming. To explain the dimming without a decreasing T_{eff} , Levesque & Massey (2020) suggest that a large-grain dust cloud passed between Betelgeuse and our line of sight, extinguishing a significant percentage of the detectable light from the star.

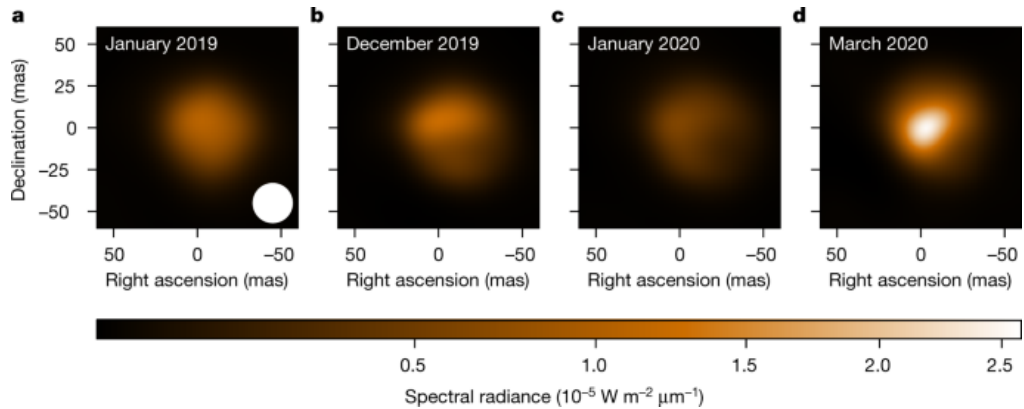


Figure 1.10. VLT/SPHERE–ZIMPOL observations of Betelgeuse before, during, and after the dimming event published by Montargès et al. (2021)). North is up; east is left. Montargès et al. (2021) enhanced the contrast using a power-law scale intensity with an index of 0.65. Observations were captured using the $Cnt - H\alpha$ ZIMPOL filter centred at 644.9 nm. The beam size of ZIMPOL is shown in observation (a) by the white disk.

The scenario of a transiting dust cloud unrelated to Betelgeuse as the source of the dimming is rejected by high angular resolution observations displaying Betelgeuse’s surface presented by Montargès et al. (2021). These observations, shown in Figure 1.10,

show that Betelgeuse's southern hemisphere became at least ten times darker than the northern hemisphere. A transiting clump of gas would appear to move across the surface of the star with observations showing the dark spot changing location in correlation to the star's varying brightness. Therefore, the transit scenario is unlikely as the dark area remained in the southwest quadrant throughout the dimming event. Though their results discount the possibility of a transiting dust cloud, Montargès et al. (2021) still attribute dust to a large portion of the dimming. This interpretation is consistent with the spectroscopic analysis by Dupree et al. (2020) which claims that the dimming is a result of dust released from a mass loss event in the year prior. The presence of dust is also inferred from speckle polarimetric observations of Betelgeuse by Safonov et al. (2020) and Cotton et al. (2020). These show signatures of enhanced Mg II emission in Betelgeuse's southern chromosphere. Dupree et al. (2020) interpret these data to suggest that a dense cloud of dust was released from the southern hemisphere of the star in the months preceding the dimming.

While they associate a decrease in temperature with the decline in brightness, Montargès et al. (2021) find that the dimming event cannot be attributed to a decrease in temperature alone despite evidence of a large cool spot in Betelgeuse's photosphere is provided by Harper et al. (2020) and Dharmawardena et al. (2020). Montargès et al. (2021) interpret these results to suggest that the observed dimming event, though aided by the cool patch observed in the photosphere, is primarily a result of a dust cloud temporarily blocking much of Betelgeuse's light. They propose the following scenario. Prior to the dimming event, a large clump of gas was released from a convection-driven cool patch in the southern hemisphere of the star's photosphere. The low temperature of the local environment caused the recently ejected gas to rapidly form dust. The resulting dust cloud temporarily obscured the southern hemisphere of the star, causing the decline in brightness seen during the Great Dimming of Betelgeuse. In all, the invocation of dust as a cause of Betelgeuse's dimming remains debatable in the field.

1.3.5 Localized Cooling of the Photosphere (No Dust)

The results presented by Harper et al. (2020) and Alexeeva et al. (2021) find evidence of a decrease in T_{eff} corresponding to the dimming event. Harper et al. (2020) present five years of Wing three filter (A, B, and C band) TiO and near-IR photometric observations of Betelgeuse, including epochs obtained during the dimming event. By comparing these data to a grid of spherical MARCS photospheric models, they find that Betelgeuse's temperature decreased by at least $\Delta T_{eff} = -125$ K between the

months of September and February, significantly lower than the value $T_{eff} = 3600 \pm 25$ K inferred by Levesque & Massey (2020). Alexeeva et al. (2021) deduce the T_{eff} by analyzing high resolution infrared spectra of Betelgeuse obtained during the dimming event. This analysis compares the strengths of temperature sensitive TiO absorption lines between 7700 and 7900 Å to synthetic MARCS models. Their results measure a temperature decrease of $\Delta T_{eff} = -170$ K.

TiO photometry from Harper et al. (2020) and sub-mm observations by Dharmawardena et al. (2020) measure an increased opacity of Betelgeuse's photosphere, providing additional evidence that dust may not be the primary cause of the dimming event. The change in opacity may best be explained by one or more cool patches, suggesting that the decrease in luminosity is instead a result of a portion of the photosphere cooling significantly. This interpretation is also consistent with the results of Kravchenko et al. (2021) who probe multiple different depths in Betelgeuse's atmosphere by applying the tomographic method to high-resolution spectral observations. They provide evidence to suggest that the propagation of two shock waves in the upper atmosphere, sustained by massive convective cells rapidly propelling gas outward, resulted in a sudden increase in Betelgeuse's molecular opacity.

Kravchenko et al. (2021) conclude that this increase in molecular opacity is best explained by a localized cool spot in the photosphere. Harper et al. (2020) provide additional evidence supporting the localized cooling hypothesis, claiming that no signatures of dust are revealed in their analysis of SOFIA-EXES spectra taken during the dimming event. This is consistent with IR photometry of Betelgeuse presented by Gehrz et al. (2020), who find no evidence of dust in their observations. These results offer further evidence for the scenario proposed by Dharmawardena et al. (2020), which concludes that the measured decrease of $\sim 20\%$ in the 450 and 850 μm sub-mm fluxes can be caused by a localized temperature decrease of $\Delta T_{eff} \geq 200$ K.

Harper et al. (2020) conclude that if the patch of the photosphere became $\Delta T_{eff} \geq 250$ K cooler than the rest of the star, no dust is required to produce the observed decrease in luminosity. Alexeeva et al. (2021) also find that their results can be reproduced without the presence of dust if the southern hemisphere of Betelgeuse was cooler than the northern hemisphere by $\Delta T \geq 250$ K. These results conclude that T_{eff} measurements derived from Betelgeuse's inhomogeneous photosphere should reveal an T_{eff} that is some combination of the multiple T_{eff} s present on the star's surface. These results provide another explanation for the observations of Betelgeuse's surface seen in Figures 1.9 and 1.10: The Great Dimming of Betelgeuse can be attributed to a large portion of the southern hemisphere decreasing in T_{eff} and thus, luminosity,

resulting in both the measured decline in brightness as well as the large dark spot observed by Montargès et al. (2021).

1.4 Motivation

Unraveling the mystery surrounding Betelgeuse’s Great Dimming Event is the primary subject of this thesis. The dimming event was carefully and continually monitored with consecutive observations at Mount Laguna Observatory (MLO). In the following section, We present five epochs of spectroscopic data that include epochs during and after the dimming event. These data contain the temperature sensitive TiO absorption feature with a bandhead at 7054 Å. While this feature is one of the best indicators of temperature for RSGs, it is unfortunately outside the range of many low resolution spectrographs. The main goal of this thesis is thus to measure Betelgeuse’s effective temperature (T_{eff}) over the course of the dimming event. The spectroscopic study in this thesis represents a unique opportunity to use the 7054 Å TiO absorption feature to probe the T_{eff} of Betelgeuse as the star’s luminosity varies.

1.5 Spectroscopic Observations

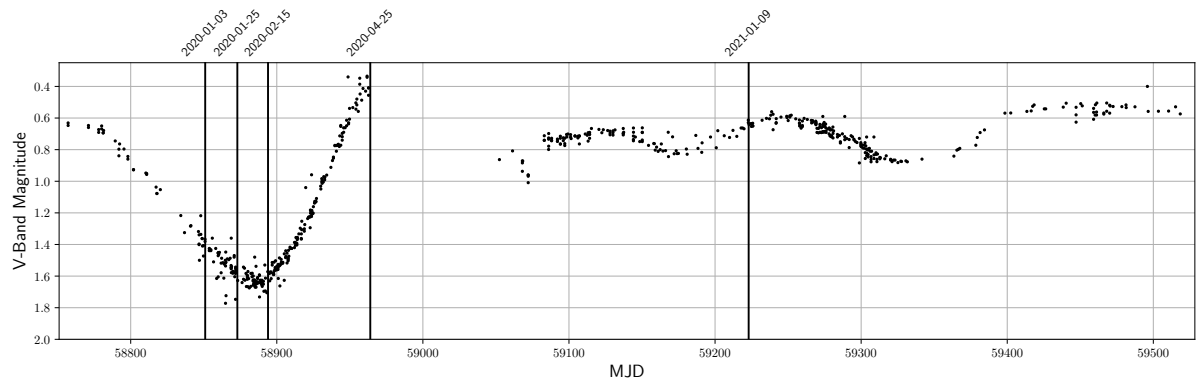


Figure 1.11. V-band lightcurve of Betelgeuse during the Great Dimming Event courtesy of AAVSO. Vertical black lines indicate epochs of the presented spectra displayed in Tables 1.3 and 1.2. Note the gap in photometric coverage following our 2020-04-25 observation due to solar conjunction.

In an effort to bring new observations to bear on the cause of the Great Dimming, we conducted spectroscopic observations of Betelgeuse with the Cassegrain spectrograph (AKA “White Spectrograph”) attached to the 1-m reflector at Mount Laguna Observatory (MLO; Smith & Nelson 1969), at five epochs that sampled the period from 3 January 2020 UT (note that UT dates are used throughout this thesis)

through 9 January 2021 UT. Details of the CCD sensor and camera are provided by Heffner (2012), which also describes the commissioning of the instrument.¹

We experimented with various gratings and tilt settings, ultimately arriving at a standard setup (hereafter referred to as the “standard setting”), used at all epochs, which employed the 300 line/mm grating at a tilt (“3390” on the dial attached to the spectrograph) that delivered a useful spectral range from roughly $5300 \text{ \AA} \rightarrow 7900 \text{ \AA}$, with $\sim 1.4 \text{ \AA/pixel}$ and a resolution of $\sim 12 \text{ \AA}$ as measured from night sky lines on long exposures. The spectrograph’s slit was always set at a position angle of 90° , and at a width corresponding to “206” units on the Vernier scale attached to the spectrograph; it is, unfortunately, unknown what physical width this corresponds to on the sky, but based on seeing estimates and visibility of sources in the guide camera is thought to be roughly 2–3”. Internal flatfields and arcs (neon and thorium-argon) were taken temporally adjacent to all science observations.

During the first three epochs, we observed Betelgeuse with additional grating tilts that served to extend the blue and/or red wavelength coverage; the first epoch also included a set of observations employing the 1200 line/mm grating, which yielded spectral coverage from $6500 \text{ \AA} \rightarrow 7200 \text{ \AA}$ at a resolution of $\sim 1.2 \text{ \AA}$. All such additional observations were simply combined with those obtained using the standard setup to extend the wavelength coverage and potentially improve the signal-to-noise ratio (SNR) in regions of overlap.

In an effort to derive an accurate relative flux calibration of Betelgeuse, we also observed flux standard stars on all nights using the same setup(s) as those used for Betelgeuse. We note though, that while we believe the relative fluxing of Betelgeuse to be quite accurate (and, certainly adequate for our science purposes), its ultimate precision is suspect at some (unknown) level since we did not align the spectrograph slit with the parallactic angle for either Betelgeuse or for the flux standard star observations.² Thus, our observations may suffer from differential light loss due to atmospheric refraction (Filippenko (1982)). However, given the relatively low air-mass of most of our observations, as well as the wide slit employed, it is not thought likely to be very significant for our observations.

Table 1.3 lists the epoch numbers, UT Date, modified Julian Date, exposure time, number of observations of Betelgeuse taken in the standard setup, airmass,

¹We note that the final observations reported by Heffner (2012) occurred on 15 February, 2010, nearly ten years prior to our first science observations of 3 January 2020; as far as we are aware, the instrument was not used in the interim.

²Note that it is technically possible, although evidently quite difficult, to alter the position angle of the spectrograph’s slit.

parallactic angle, and the flux standard star used for each of the five epochs. All spectroscopic data were uniformly reduced by Prof. Douglas Leonard, following procedures detailed by Leonard et al. (2000). Briefly, all one-dimensional sky-subtracted spectra were extracted optimally (Wade & Horne (1988)) in the usual manner, generally with a width of $\sim 9''$ along the slit, although this was modified based on seeing conditions (usually a width of at least ~ 5 times the seeing was employed). Each spectrum was then wavelength and flux calibrated, as well as corrected for continuum atmospheric extinction and telluric absorption bands (Wade & Horne (1988); Bessell et al. (1998); Matheson et al. (2000)).

Due to the very short exposure times given the brightness of Betelgeuse, we typically observed Betelgeuse dozens of times in rapid succession at every epoch. All such spectra were then combined with equal weighting for the standard setting; for the first three epochs, in which additional settings were employed, the additional spectra were combined in the overlap regions and then added to the ends to extend the wavelength range of the final spectrum.

There were two issues encountered during the reductions. First, significant “fringing” was observed in all observations redward of $\sim 6500 \text{ \AA}$. Despite attempting to mitigate this through multiple techniques — e.g., using dome or sky flats instead of internal flats, adjusting the order of the normalization to the flats, spectrally shifting the flatfields, using no flatfields at all, or fitting the fringes in the flux standard star — we were unable to achieve any results that were superior to simply flattening using the local internal flats. Fortunately, our primary science goal — measuring the equivalent width of a feature several hundreds of Angstroms wide — is largely unaffected by fringing considerations.

Second, we found that the wavelength solutions ultimately applied on different nights (or, even, portions of an individual night) were frequently offset from each other by up to several Angstroms. Heffner (2012) noted that the absolute wavelength scale derived from local arc exposures with this camera suffers from zero-point errors, likely due to at least two factors. First, the optical path of starlight through the spectrograph differs from that of the internal comparison lamps. Second, there is substantial hour-angle-dependent flexure of the lens that is used as the spectrograph camera. Although our science analysis does not depend crucially on a highly accurate wavelength scale, we decided to carry out the following procedure to place all of our spectra on a common wavelength scale prior to analysis. First, we measured the location of the H α absorption feature at each epoch. Next, we linearly shifted the final spectrum from each epoch so that this feature fell at 6563.31 \AA , the nominal value for

the established radial velocity of Betelgeuse of +21 km/s (Mathias et al. (2018)). As a final check, we then cross-correlated each epoch’s final, shifted spectrum against the spectrum obtained in Epoch 4 (Table 1.3), and confirmed that none had a cross-correlation peak of more than 0.4 Å.

We present our final spectrum for each of the five epochs in Figure 1.12. Observations are outlined in Table 1.2. Figure 1.11 shows the location of our epochs on Betelgeuse’s AAVSO³ V-band Light curve.

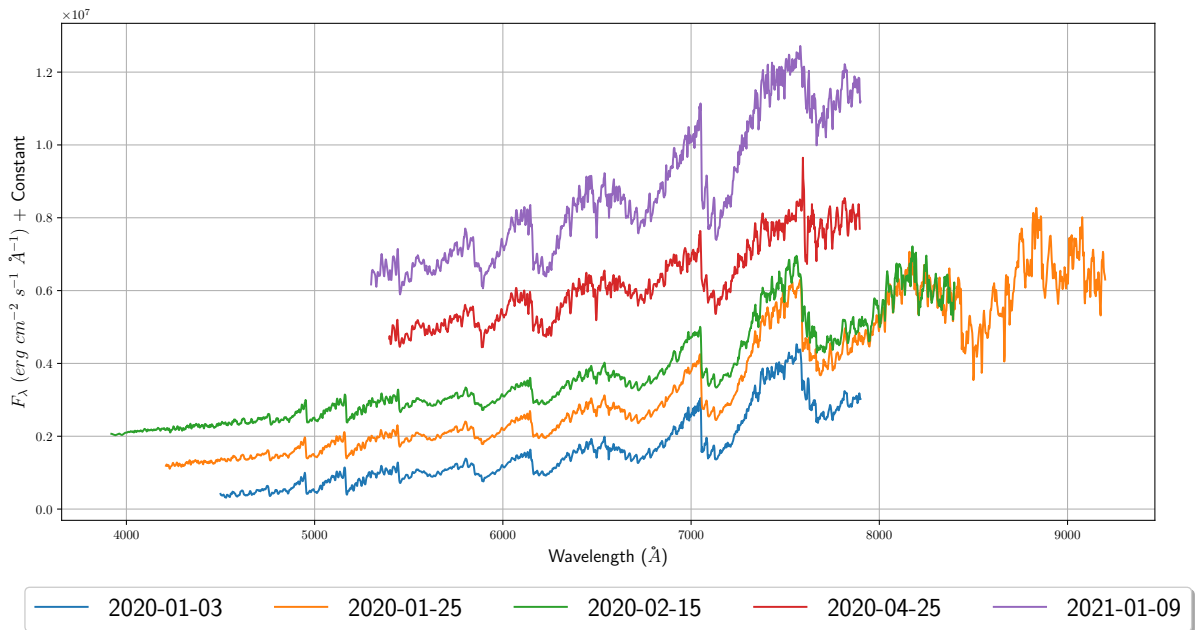


Figure 1.12. Final spectrum for each of the five epochs of observation outlined in Tables 1.3 and 1.2.

Date	MJD	m_V
2020-01-03	58,851.3	1.40 ± 0.03
2020-01-25	58,873.2	1.58 ± 0.02
2020-02-15	58,894.2	1.58 ± 0.01
2020-04-25	58,964.1	0.42 ± 0.03
2021-01-09	59,223.3	0.64 ± 0.01

Table 1.2. Journal of spectroscopic observations of Betelgeuse obtained at MLO. Displayed are the calendar date, Modified Julian Date (Julian Date - 2400000.5), and estimated V-band magnitude of Betelgeuse at each epoch. Each epoch’s V-band magnitude and corresponding uncertainties were derived by averaging over the available AAVSO data in bins of ten days each.

³Photometric lightcurves provided by AAVSO are available at <https://www.aavso.org/>

Table 1.3. Journal of Spectroscopic Observations of Betelgeuse

UT Date ^c	MJD ^d	Total Range ^a (Å)	Exposure ^b (s)	Air Mass	Parallactic Angle (deg) ^e	Flux Standard
2020-01-03.3	58,851.3	4500–7900	2.0 (50)	1.12	161	HD 19445
2020-01-25.2	58,873.2	4210–9200	0.7 (48)	1.13	156	HR 3454
2020-02-15.2	58,894.2	3920–8400	1.0 (30)	1.13	24	HR 3454
2020-04-25.1	58,964.1	5396–7896	0.5 (50)	1.87	56	HR 3454
2021-01-09.3	59,223.3	5300–7900	0.3 (95)	1.11	170	HR 3454

Note - All observations reported here were obtained with the Cassegrain spectrograph on the 40" telescope at Mount Laguna Observatory using the 300 line/mm grating; additional details about the observations are given in §1.5. The spectrograph's slit was always set at a position angle of 90°.

^aTotal range of useable spectrum.

^bExposure time in seconds for each individual observation taken in the standard setting (§1.5), with total number of exposures taken in the standard setting shown in parenthesis.

^cyyyy-mm-dd.d

^dModified Julian Date (Julian Date - 2400000.5).

^eParallactic angle (Filippenko 1982) at the time of the exposures taken in the standard setting; all observations taken with the slit at a position angle of 90°.

CHAPTER 2

Methods

2.1 Estimating the Effective Temperatures of Red Supergiants

Fully understanding the extreme nature of RSGs is a compelling challenge, as decryption of their complicated behavior reveals vital hints regarding the late stages of stellar evolution. Effective temperature (T_{eff}) is perhaps the single most important property in describing the surface features of a RSG, yet attempts to confidently measure this value are met with significant hurdles. An accurate determination of this parameter is necessary for correctly placing a RSG on the H-R diagram. While the location of any given star on the abscissa of an H-R diagram is dictated by its T_{eff} , RSG luminosities are intensely temperature sensitive. Therefore H-R diagram placement on the y-axis is heavily reliant on T_{eff} as well. RSGs have massive extended atmospheres and are the coldest members of the high-mass star population. As a result of their low temperatures, determining the bolometric luminosity (M_{bol}) for a RSG requires substantial T_{eff} -dependant bolometric corrections for standard *UBVRI* photometry (Massey (1998)).

Bolometric corrections are derived by comparing stellar atmosphere models to observational data. Synthetic stellar spectra did not accurately represent these stars until recently. RSG T_{eff} scales in the past were created under the assumption that the spectrum of these stars could be modeled with a blackbody continuum. The low T_{eff} inherent to these stars propagates to a spectrum dominated by molecular absorption lines. The spectrum of a RSG is thus poorly represented by a blackbody continuum, and the molecular lines require that evolutionary models carefully and correctly represent the accompanying molecular opacities (Levesque et al. (2006)). The unreliable bolometric corrections that followed cascaded into large inaccuracies. Since RSGs can range in T_{eff} from 3400 – 4500 K, temperature-dependant bolometric corrections can vary by nearly 2 magnitudes. For example, a 10% error in the measured T_{eff} corresponds to a factor of 2 error in V-band derived M_{bol} values (Levesque et al. (2005)). The sensitivity of luminosity derivations to temperature makes an accurate T_{eff} critically important when plotting the position of a RSG on both axes the H-R diagram. Poor H-R diagram placement caused by inaccurate T_{eff} scales are a

significant reason that stellar evolutionary models predicting the behavior of RSGs frequently disagreed with observations until recently.

One of the first complications was the dearth of available observational data. There are very few nearby Galactic RSGs and the small number of nearby stars often present another observational obstacle. Nearby high mass RSGs are difficult to observe. They are often too bright and saturate the detectors of high precision instruments (Levesque (2017)). Another challenge is caused by extinction (A_V). Both interstellar and circumstellar foreground dust can cause these stars to falsely appear cooler. Thoroughly accounting for A_V is further complicated by the frequent mass loss events associated with RSGs. It is difficult to differentiate between interstellar and circumstellar material as the source of extinguished light. Additional challenges in mapping observational data to T_{eff} arise as a result of uncertain radius derivations caused by the complicated and variable atmospheres of RSGs (Davies et al. (2013)).

The difficulties in constraining the radii of RSGs discussed in §1.2.1 hinder T_{eff} derivations reliant on the Stefan–Boltzmann formula:

$$L_\star = 4\pi R_\star^2 \sigma_{sb} T_{eff}^4$$

Here, σ_{sb} is the Stefan-Boltzmann constant, while L_\star and R_\star represent the stellar luminosity and radius, respectively. The inferred radius of a RSG is highly sensitive to the observed wavelength. Spectral regions of high opacity caused by strong molecular lines result in the star appearing much larger when compared to other spectral regions. Furthermore, atmospheres of RSGs are populated by massive convective cells. These cells cause RSGs to have an asymmetrical photosphere and poorly defined radius. These extended and asymmetric atmospheres do not match well with predictions that rely on plane-parallel assumptions for stellar atmospheres. Furthermore, the radii of RSGs can vary drastically over time, causing further complexities in radius determinations. These variations can also cause the surface gravity (\log_g) to fluctuate rapidly and unexpectedly (Davies & Beasor (2020)).

The earliest efforts used interferometric data of a few nearby low-mass galactic RSGs that were dim enough to observe. These methods proved inaccurate due to inconsistent radius measurements resulting in T_{eff} correlations that did not scale well towards higher mass and extragalactic RSGs (Davis (1997)). Attempts at correlating the broadband ($B - V$) color to temperature revealed that the multitude of weak metal lines contained within the range of the B photometric passband are highly sensitive to \log_g . Frequent variations in radius (and thus \log_g) make this method an inaccurate gauge of T_{eff} . Early efforts at correlating V-band magnitudes to T_{eff} were promising, as there was a noticeable correlation between the two. However, observed variation in the

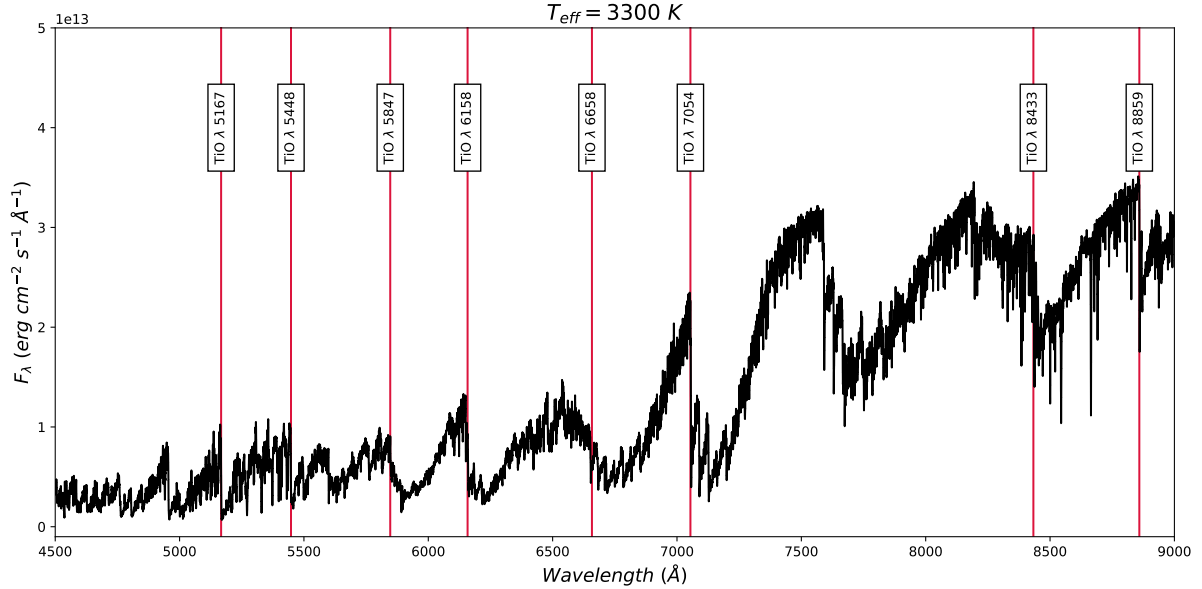


Figure 2.1. Notable spectral features shown on the synthetic PHOENIX SED of a Red Supergiant with $T_{eff} = 3300$ K, courtesy of Husser et al. (2013). Red vertical lines correspond to the bandhead of each TiO absorption feature used in determining the spectral types of RSGs.

V-magnitude is not solely a result of a changing T_{eff} . Phenomena commonly displayed by RSGs cause discrepancies in V-band magnitude reliant T_{eff} relations. Radial pulsations, mass loss events, and convective activity can all appear as variability in the apparent V-band magnitude. Therefore, a change in the observed V-band magnitude of a RSG cannot be immediately attributed to a change in T_{eff} (Levesque (2017)).

Since many classic methods of measuring a star's T_{eff} are not accurate when applied to RSGs, creating a T_{eff} scale requires a novel visual or spectroscopic property that is sensitive to changes in temperature but unaffected by their complicated upper atmospheres. Therefore, calculations of T_{eff} require the comparison of spectrophotometric data to stellar atmosphere models (Levesque (2010)). The 2003 MARCS stellar atmosphere models from Gustafsson et al. (2003) were the first to accurately predict the effect of oxygen-rich molecules on the opacity of these stars at different wavelengths. This allowed for the first accurate RSG T_{eff} scales.

The spectral type of RSGs such as Betelgeuse is determined using the broad absorption bands of TiO. The most notable of these absorption bands appear at 4761 Å, 4954 Å, 5167 Å, 5448 Å, 5847 Å, 6158 Å, 6658 Å, and 7054 Å. Notable spectral features are displayed on a PHOENIX model SED with $T_{eff} = 3300$ K in Figure 2.1. These easily identifiable spectral lines have useful applications independent of spectral classification. By comparing the 2003 MARCS stellar atmosphere models to

observational data, Levesque et al. (2005) derived a correlation between T_{eff} and the TiO absorption bands, showing that the strength of TiO bands are an accurate T_{eff} indicator in RSGs. The TiO band at 7054 Å is particularly sensitive to temperature while only showing minor correlations with \log_g (Levesque (2017)). Measuring the line strength of this feature is a well established method of measuring the correlation between line strength and temperature (Gustafsson et al. (2003)). However, many spectra obtained of RSGs do not fully cover the 7054 Å feature due to limited spectral range. For derivations lacking this feature, the most common methods in determining RSG $T_{eff}s$ via spectroscopy entail comparing the line strengths of multiple available TiO features. In this thesis, I present estimates of Betelgeuse's T_{eff} during and after the Great Dimming event derived by comparing the observed 7054 Å line strength to a selected grid of synthetic PHOENIX model spectra; to my knowledge, this is the first time that this has been done.

2.2 Model Atmospheres and Spectra

The 2003 MARCS stellar atmosphere models proved useful in precisely describing the concrete relation between TiO molecular features in the SED of a RSG and its T_{eff} for the first time. However, the PHOENIX stellar atmosphere models developed by Husser et al. (2013) show better agreement with observed TiO band strengths for galactic RSGs (Davies et al. (2013)). The first PHOENIX library, published in 1995 by Allard & Hauschildt (1995), consisted of 700 M-dwarf model atmospheres derived under the assumption of local thermodynamic equilibrium. The library was greatly expanded through the efforts of Hauschildt et al. (1999), which added model atmospheres of giant and supergiant M-type stars with $T_{eff}s$ ranging from 3000 K to 6000 K.

In the decades since PHOENIX's development, the catalog has been significantly upgraded. The calculations presented in this thesis compare observed spectral energy distribution functions (SEDs) of Betelgeuse to a series of synthetic spectra derived from PHOENIX spherical local thermodynamic equilibrium (LTE) model atmospheres (Husser et al. (2013)). This catalog includes an updated equation of state for cool stars as well as an up-to-date atomic and molecular line list. Combined, these upgrades better account for the complicated atmospheres of cooler stars, producing spectra which match observations significantly better than other synthetic libraries. These properties result in the PHOENIX spectral library being the best modern library in the modeling of cool, high-mass stars, such as Betelgeuse.

The selected grid of synthetic PHOENIX spectra¹ was chosen to best match derived values for Betelgeuse. A series of synthetic spectra was selected for comparison, with $T_{eff}s$ ranging from 3300 to 4000 K. The step size is 100 K. These synthetic spectra have surface gravity $\log_g = 0.0$ cm/s². The chosen metallicity [M/H] for this study is 0.0. Synthetic spectra have an alpha element enhancement [α /Fe] of 0.0. These values are chosen in accordance to the best fitting values of multiple Betelgeuse spectroscopic investigations, including investigations by Levesque & Massey (2020), Levesque et al. (2005), Montargès et al. (2021), and Alexeeva et al. (2021).

2.3 Measuring Equivalent Widths

This study probes Betelgeuse's T_{eff} over multiple epochs during and after the Great Dimming event by comparing the observed intensity of the TiO absorption band at 7054 Å to the selected grid of synthetic model spectra. The strength of an absorption feature can be quantitatively represented by its equivalent width (W_λ). W_λ is calculated by measuring the width of a rectangle containing the same area as the spectral feature with a height equal to that of the continuum emission surrounding the spectral feature. A visual representation of W_λ can be seen in Figure 2.2. The formula used to calculate W_λ is:

$$W_\lambda = \int_{\lambda_1}^{\lambda_2} \frac{F_c - F_\lambda}{F_\lambda} d\lambda \quad \text{or} \quad W_\lambda = \int_{\lambda_1}^{\lambda_2} \left[1 - \frac{F_\lambda}{F_c} \right] d\lambda \quad (2.1)$$

Here, F_λ is the flux in the feature at wavelength λ , while F_c is the flux of the continuum at λ . The observed feature's lower and upper wavelength limits are λ_1 and λ_2 . The wavelength step size is represented by $d\lambda$. The units of W_λ are the same as that of λ . In practice, it is common to use an expression for W_λ that creates a profile of the feature which accounts for the surrounding continuum. SEDs are also not continuously measured wavelengths, but instead are a compilation of energy measurements taken by individual pixels which correspond to a wavelength interval. Thus, a summation replaces the integration. Both can be accomplished by numerically integrating equation 2.1 and applying the mean value theorem, which obtains the formula:

$$W_\lambda = \Delta\lambda \left| \sum_{n=\lambda_1}^{\lambda_2} \left[1 - \frac{F_\lambda}{F_c} \right] \right| \quad (2.2)$$

¹The library of PHOENIX stellar atmospheres and synthetic spectra by Husser et al. (2013) can be downloaded from their homepage, <http://phoenix.astro.physik.uni-goettingen.de/>

Here the wavelength interval $\Delta\lambda = \lambda_2 - \lambda_1$. Equation 2.2 normalizes the flux of the feature by the continuum, therefore isolating the feature in the summation (Vollmann & Eversberg (2006)).

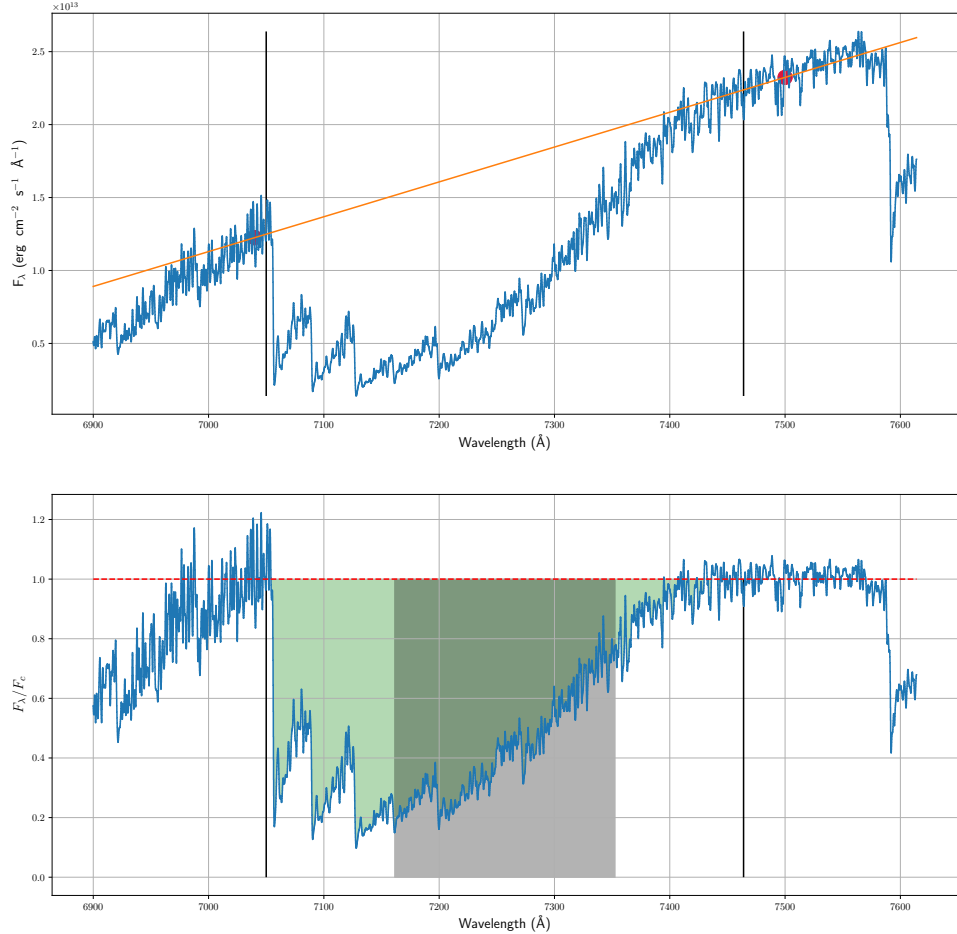


Figure 2.2. The process used to measure W_λ , as detailed in §2.3 and §2.4 Top: F_c and the selected feature, with points used to calculate F_c shown via the red dots. The horizontal width of the grey shaded area corresponds to the measured W_λ . The shaded grey area has the same area as the line strength, shown in green. This process for the entire grid of synthetic PHOENIX spectra used in this thesis are shown in Figures A.1 and A.2). The same procedure was also applied to the data of Betelgeuse.

W_λ is a useful representation as it directly corresponds to the strength of an absorption feature. It is not synonymous with the actual width of a feature nor its full width at half maximum (FWHM). By definition, W_λ is a positive value for absorption features and negative when applied to emission lines. Thus, W_λ is rarely used in

describing emission features. W_λ precisely measures the fraction of energy removed from the spectrum by the absorption feature, regardless its shape, and derivations are not affected by a spectrograph's resolution. Therefore, all measurements of W_λ are directly comparable. Thus no corrections are necessary to compare W_λ values of the same feature obtained with different equipment as well as values derived from synthetic spectra (Carroll & Ostlie (2006); Dicenzo & Levesque (2019)).

2.4 Line Selection and Features

The TiO absorption feature with a bandhead at $\lambda = 7054 \text{ \AA}$ is chosen with the intention of mapping its W_λ values to T_{eff} . Selection of this feature is motivated by its previously mentioned benefits, most importantly the fact that this feature is highly sensitive to T_{eff} , but relatively insensitive to uncertainties in surface gravity, metallicity, or alpha element abundances. Cooler RSG produce larger values of W_λ for the 7054 \AA TiO feature, as the line strength increases as T_{eff} decreases. The lower and upper wavelength limits λ_1 and λ_2 are 7050 \AA and 7464 \AA , respectively (Dicenzo & Levesque (2019)). A spectrum taken from our data on 2020-02-15 is shown in Figure 2.3 which serves to highlight the full range of the TiO feature at 7054 \AA .

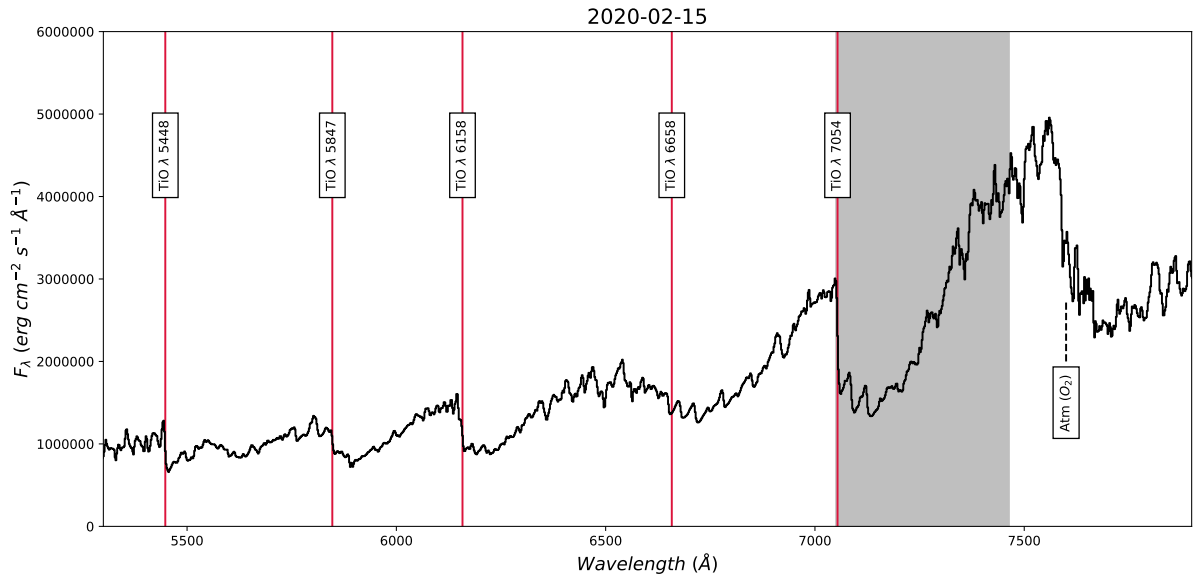


Figure 2.3. The spectrum of Betelgeuse obtained on 2020-02-15 with prominent spectral features labeled. Red vertical lines correspond to the temperature sensitive TiO absorption features. The grey shading displays the full wavelength range of the 7054 \AA TiO feature. The location of the O_2 telluric feature (i.e., the A-band) is marked by a dotted vertical line.

Extra care must be taken when isolating the 7054 Å TiO absorption feature. The absorption feature spans ~ 400 Å and does not have a smooth, easily defined continuum on either end. F_c is estimated by fitting a straight line between two selected points on either side of the feature in order to accurately characterize both the red and blue portions of the surrounding continuum. These points are selected quantitatively. Each point corresponds to the median flux value of continuum within 150 Å of λ_1 and λ_2 , chosen to carefully avoid including the absorption feature itself while being close enough to accurately measure its surrounding continuum. F_c as a function of λ is derived by fitting a line between these two points. Figure 2.2 displays this process in detail. This method applied to the entire grid of selected model spectra is shown in Figures A.1 and A.2.

W_λ (Å)	T_{eff} (K)
191	3300.0
169	3400.0
130	3500.0
94	3600.0
67	3700.0
46	3800.0
35	3900.0
26	4000.0

Table 2.1. Equivalent Widths of the 7054 Å TiO absorption feature measured in PHOENIX MODEL SEDs

Date	W_λ (Å)	σ_{W_λ}
2020-01-03	117	1.22
2020-01-25	118	1.06
2020-02-15	119	2.33
2020-04-25	72	1.70
2021-01-09	89	1.81

Table 2.2. Multi-epoch equivalent width measurements of Betelgeuse’s 7054 Å TiO absorption feature with uncertainties.

The 7054 Å TiO absorption feature W_λ measurements are shown in Tables 2.1 and 2.2 for all data collected as a part of this thesis. Table 2.1 displays values of W_λ derived from the PHOENIX model spectra. The process for deriving W_λ values for all Betelgeuse Epochs is shown in 2.4 and the resulting values are shown in Table 2.2.

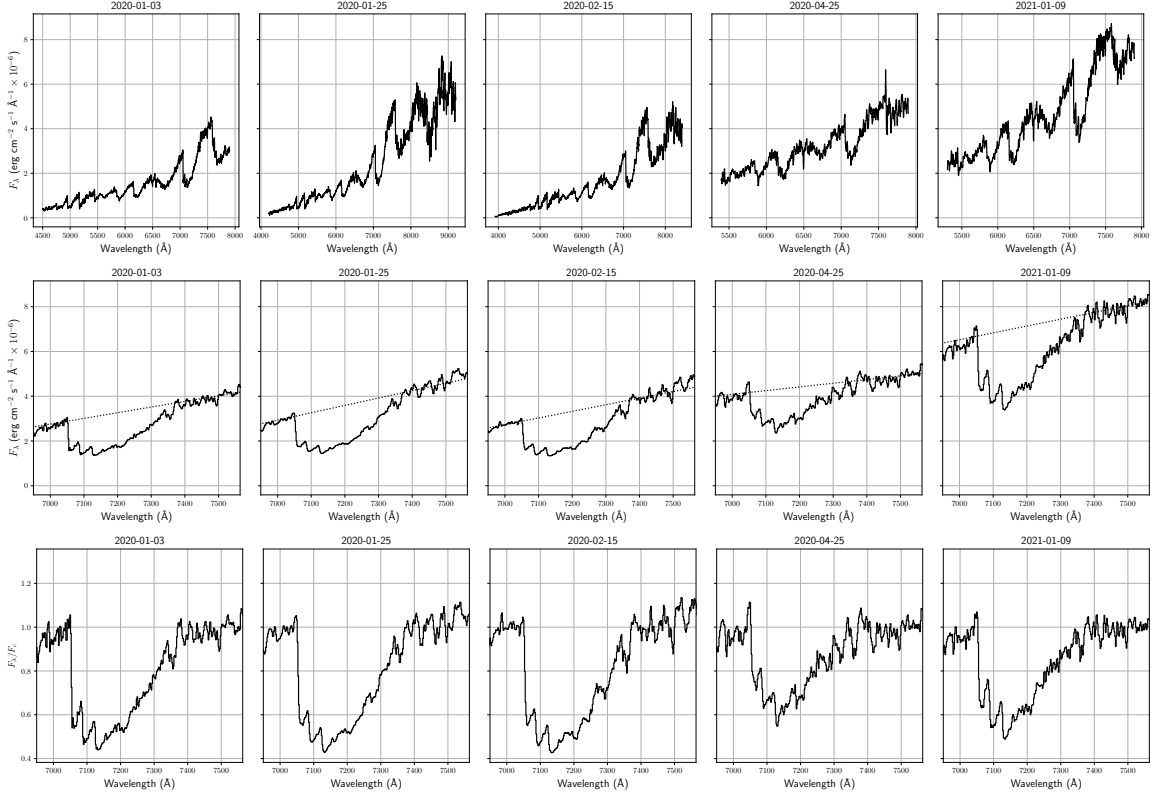


Figure 2.4. Top: Spectroscopic observations of Betelgeuse. Middle: Each epoch’s 7054 Å TiO band with the dotted line corresponding to F_c . Bottom: The normalized 7054 Å TiO for each epoch, displaying clear variations in strengths. It is worth noting the obvious qualitative difference in the strength of this feature between the epochs taken during Betelgeuse’s historic minimum (first three epochs) and those taken after it had regained its normal luminosity (final two epochs).

2.5 Calibration of the Equivalent Width-Effective Temperature Relation

A quantitative correlation between the W_λ of a RSG’s 7054 Å TiO absorption feature and its T_{eff} is derived using values obtained from the grid of synthetic PHOENIX SEDs. These measurements are shown in Table 2.1. They include W_λ measurements corresponding to RSGs with an T_{eff} range of 3300 to 4000 K in increments of 100 K. The relation is calculated by applying a 1-D linear interpolation to these data. This is a method of polynomial curve fitting that uses linear polynomials to fit a straight line between each pair of points (Mészáros & Prieto (2013)). This quantitatively maps W_λ to T_{eff} for RSGs within the selected T_{eff} range. This fit is shown in Figure 2.5. Each epoch’s T_{eff} is then measured by fitting observed values of W_λ to the derived scale. The resulting fits are shown in Figure 2.5.

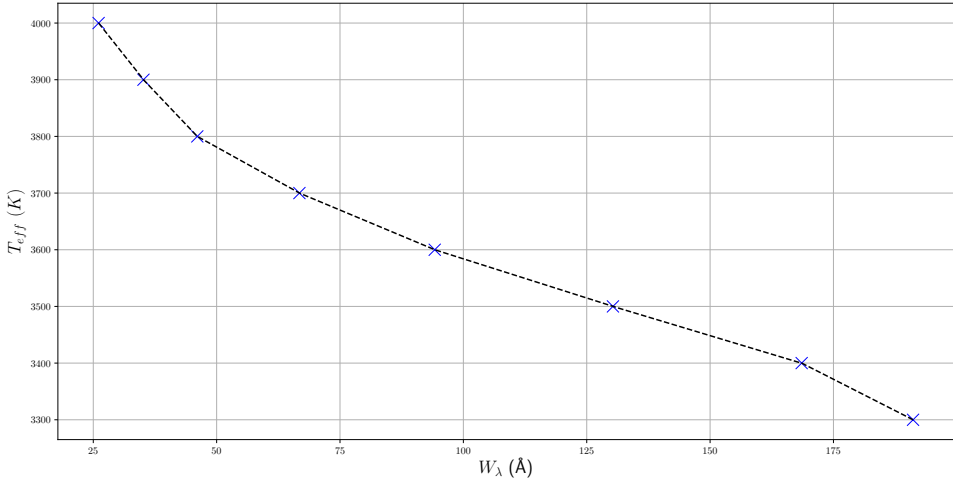


Figure 2.5. Relation between T_{eff} and W_λ derived from PHOENIX synthetic spectra.

2.6 Establishing a Correlation between V-band Magnitude and Effective Temperature from Models

Investigating if a change in effective temperature alone can reasonably explain the change in V-band magnitude (ΔM_V) observed during the Great Dimming event is the primary motivation of this thesis. The change in Betelgeuse's effective temperature, ΔT_{eff} , is measured by applying the RSG T_{eff} diagnostic described in §2.5 to multi-epoch spectroscopic observations. Synthetic photometry of the PHOENIX model atmospheres is used to test if the ΔT_{eff} inferred for Betelgeuse from our spectroscopic observations can reproduce the Great Dimming event's observed ΔM_V . Synthetic photometry describes methods of convolving model atmosphere fluxes to magnitudes of standard passbands (Straizys (1996)). These methods are used to convert ΔT_{eff} into an expected ΔM_V by calculating values of M_V corresponding to each SED in the grid of PHOENIX model spectra. The expected values of ΔM_V can be compared with inferred ΔM_V derived from spectra observed over the Great Dimming event.

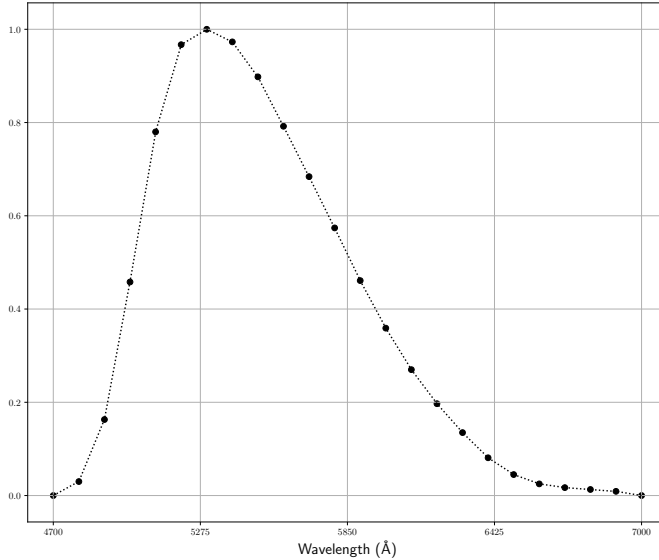


Figure 2.6. Sensitivity Function for the V-passband as a function of Wavelength λ from Bessell (1990). Tabulated values for the sensitivity function are shown in Table 2.3.

Synthetic photometry methods used to compute V-band magnitudes from model SEDs are in accordance with modern synthetic UBVRI conversions described by Bessell (1990). Further updates and clarifications to these methods have since been published, including Bessell et al. (1998), Bessell (1999), Bessell (2005). Given a passband with a wavelength range of $\lambda_1 \leq \lambda \leq \lambda_2$, the number of detected photons across the passband is known as the integrated flux F_S . Computing F_s in units of $\text{ergs cm}^{-2} \text{ s}^{-1} \text{ Å}^{-1}$ uses the following formula:

$$F_S = \int_{\lambda_1}^{\lambda_2} (\lambda F_\lambda) \left(\frac{R_\lambda}{\lambda} \right) d\lambda \quad (2.3)$$

Where F_λ is the flux at wavelength λ in units of $\text{ergs cm}^{-2} \text{ s}^{-1} \text{ Å}^{-1}$. Fluxes are weighted by wavelength through the sensitivity function R_λ . An example of the V-passband convolution on a PHOENIX synthetic spectrum is displayed in Figure 2.7. The derived value of F_s can then be converted to the selected band's synthetic magnitude. Recall, that for two stars with fluxes F_1 and F_2 , the difference between their magnitudes M_1 and M_2 can be expressed by the formula:

$$M_1 - M_2 = -2.5 \log_{10} \left(\frac{F_1}{F_2} \right) \quad (2.4)$$

λ	V
4700	0.000
4800	0.030
4900	0.163
5000	0.458
5100	0.780
5200	0.967
5300	1.000
5400	0.973
5500	0.898
5600	0.792
5700	0.684
5800	0.574
5900	0.461
6000	0.359
6100	0.270
6200	0.197
6300	0.135
6400	0.081
6500	0.045
6600	0.025
6700	0.017
6800	0.013
6900	0.009
7000	0.000

Table 2.3. Tabulated values for the standard V-passband sensitivity function for each wavelength λ from Bessell (1990).

The selected passband's synthetic magnitude M_s can thus be computed from F_s and a standard star acting as zero-point (ZP) with known fluxes and magnitudes to include for F_{ZP} and M_{ZP} . M_s is computed by applying these terms to formula 2.4 as follows:

$$M_s = -2.5 \log_{10} \left(\frac{F_s}{F_{ZP}} \right) + M_{ZP} \quad (2.5)$$

In §2.5, we derived a quantitative relationship between the W_λ of the TiO absorption feature at 7054 Å and T_{eff} . The described synthetic photometry methods are applied to investigate if Betelgeuse's inferred ΔT_{eff} can reproduce observed values of ΔM_V . The V-passband sensitivity function is provided by Bessell (1990). The V-passband has a wavelength range of 4700 Å to 7000 Å. Figure 2.6 displays R_λ derived from the V-passband response function shown in Table 2.3. For completeness, Vega

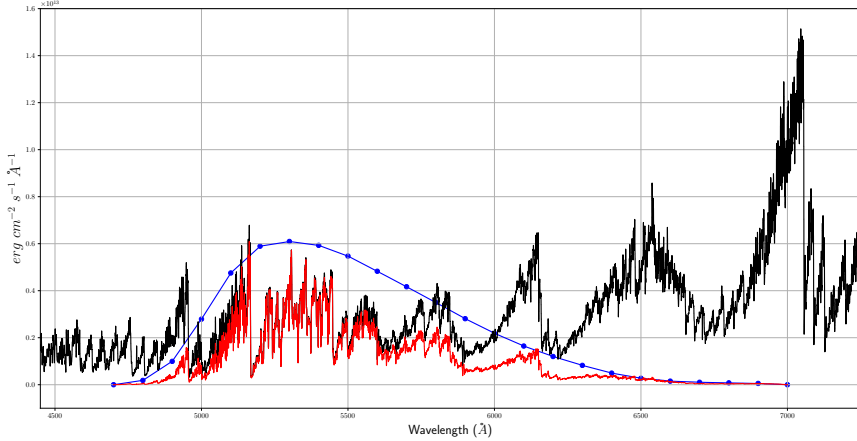


Figure 2.7. V-passband photometric convolution of a PHOENIX synthetic SED. The dotted blue curve displays sensitivity function shown in Figure 2.6. The red SED displays the recorded weighted passband.

derived ZP values F_{ZP} and M_{ZP} are included in the derivation². However, it should be noted that the choice in ZP values is inconsequential to the results as this investigation is focused on deriving the *change* in V-band magnitude, ΔM_V , rather than individual measurements of M_V .

A 1-D linear interpolation is applied to these results to create a finer scaling between ΔT_{eff} and ΔM_V . The relation between ΔM_V and ΔT_{eff} derived using these values is displayed in Figure 2.8. Changes in the V-band magnitude ΔV and inferred values of ΔT_{eff} , are defined hereafter as $\Delta V \equiv (V_T - V_{T_0})$ and $\Delta T_{eff} \equiv (T - T_0)$ respectively. Here, $T_0 \equiv 3678$ K; motivation behind the selection of T_0 is provided in §3.1.

²For the V-passband, Vega's integrated flux $F_{ZP} = 3.631 \times 10^{-13}$ ergs cm $^{-2}$ s $^{-1}$ \text{\AA} $^{-1}$, while the ZP magnitude $M_{ZP} = 0.008$. (Bessell (1990))

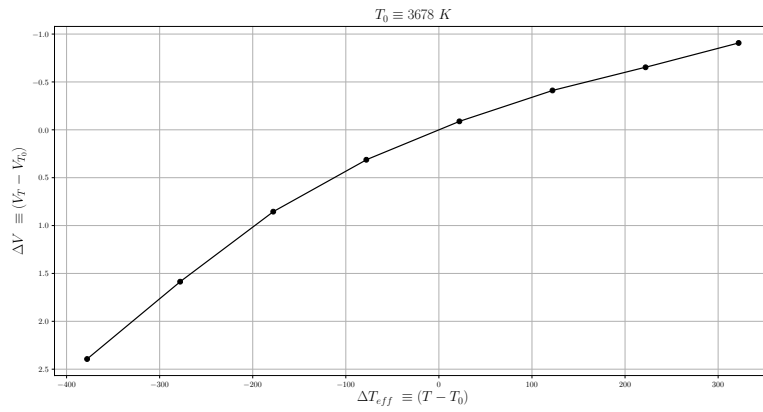


Figure 2.8. ΔM_V as a function of ΔT_{eff} derived by applying the synthetic photometry methods detailed in §2.6. The motivation for choosing $T_0 \equiv 3678 \text{ K}$ is elaborated on in §3.1.

Date	W_λ (Å)	T_{eff} (K)	M_V
2020-01-03	117 ± 1.22	3534 ± 3.0	1.40 ± 0.03
2020-01-25	118 ± 1.06	3533 ± 3.0	1.58 ± 0.02
2020-02-15	119 ± 2.33	3529 ± 6.0	1.60 ± 0.01
2020-04-25	72 ± 1.70	3678 ± 6.0	0.47 ± 0.03
2021-01-09	89 ± 1.81	3617 ± 7.0	0.65 ± 0.03

Table 3.1. Epoch of observation, measured equivalent width of the 7054 Å feature, derived effective temperature, and observed V-band magnitude of Betelgeuse. The methods used to calculate W_λ and T_{eff} are described in §2.3 and §2.5, respectively. For each epoch, Betelgeuse’s V-band magnitude M_V and corresponding uncertainty is derived by averaging over the available AAVSO data in bins of ten days each. These results correspond to those presented in Figure 3.3

CHAPTER 3

Results

3.1 Betelgeuse’s Effective Temperature Estimated from Observed Spectra

Each epoch’s T_{eff} is inferred by fitting values of the 7054 Å TiO absorption feature’s W_λ to the theoretical scaling relations detailed in §2.5. This process is displayed in Figure 3.3 and the results are listed with uncertainties in Table 3.1, which include data obtained during (first three epochs) and post-dimming (final two epochs). The statistical uncertainty in each epoch’s reported W_λ is derived by measuring the 7054 Å feature’s W_λ for every spectroscopic observation used in the creation of each night’s final science spectrum (Table 1.3), and then computing the standard deviation of the spread in the measured values. It should be noted that these results assume that the PHOENIX provide accurate SED representations for each individual T_{eff} without systematic errors¹. The uncertainty in W_λ is propagated to T_{eff} by computing the potential range in T_{eff} ’s encapsulated by the W_λ uncertainty.

Our results show that when Betelgeuse recorded its faintest apparent magnitude, it also recorded its coolest effective temperature. On 2020-02-15, when Betelgeuse is just post-minimum, we measure that $T_{eff} = 3529 \pm 6.0$ K. Conversely, on 2020-04-25,

¹While systematic uncertainties are most likely present in the model data, they are difficult to quantify as the exact chemical composition of these stars are not perfectly constrained (Husser et al. (2013).)

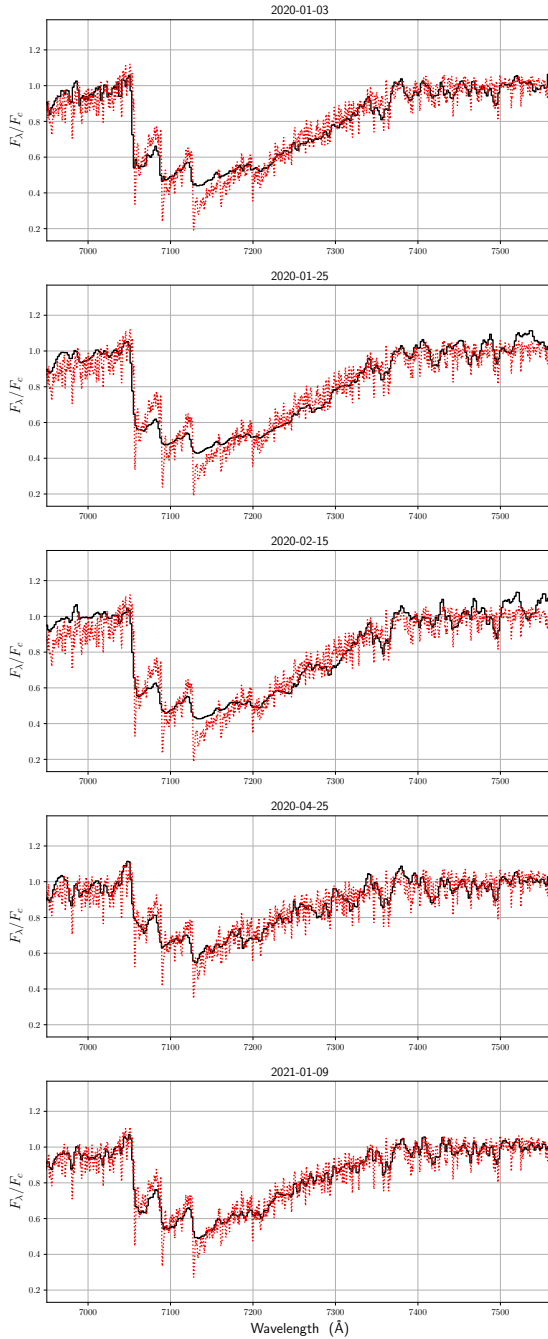


Figure 3.1. Observed and theoretical spectra. The black spectra displays the normalized 7054 Å TiO feature for each epoch. The red spectrum shows the normalized 7054 Å TiO feature corresponding to a synthetic spectra with the same T_{eff} as inferred for each epoch. The red spectrum is derived from synthetic PHOENIX models via a weighted arithmetic mean. It should be noted that the resolution of the model spectra is much finer than the resolution of the spectra observed for Betelgeuse. This causes the synthetic spectra to display many more dips and rises than the observed spectra.

the brightest recorded apparent magnitude corresponds to the highest T_{eff} of $T_{eff} = 3678 \pm 6$ K. These results suggest a positive correlation between our inferred T_{eff} and observed V-band magnitude M_V : The hotter the star, the brighter it appears. The logical question to pursue then becomes: Can the change in T_{eff} completely explain the resulting observed change in M_V ?

We found that Betelgeuse increased in temperature by 149 ± 12 K between the epochs of 2020-02-15, and 2020-04-25, which is the largest temperature increase measured in this study. Figure 3.2 shows inferred values of T_{eff} and W_λ in context with the photometric V-band lightcurve observed over the course of the Great Dimming

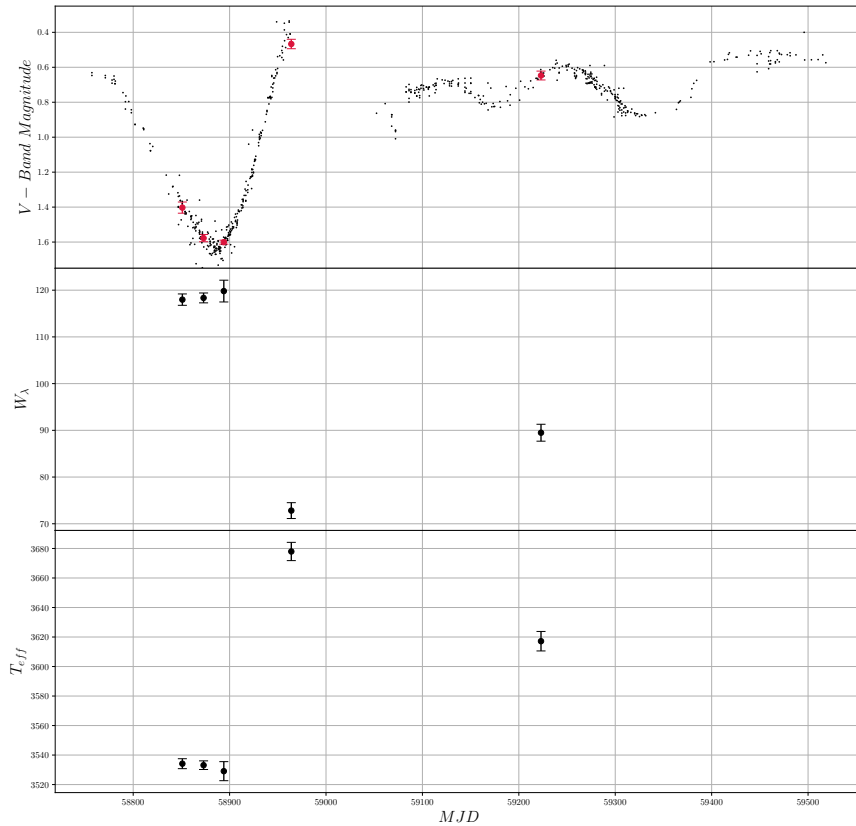


Figure 3.2. Top: The Mean V-band Magnitude for each epoch, shown in red, compared to the photometric V-band lightcurve observed during the Great Dimming event. Middle: Each epoch's measured W_λ . Bottom: Inferred values of Betelgeuse's T_{eff} for each epoch, derived from the TiO 7054 Å W_λ relation (§2.5). Values of W_λ and T_{eff} are derived from spectra obtained on 2020-01-03, 2020-01-25, 2020-02-15, 2020-04-25, and 2021-01-09. Calculating uncertainties for W_λ and T_{eff} is described in §3.1.

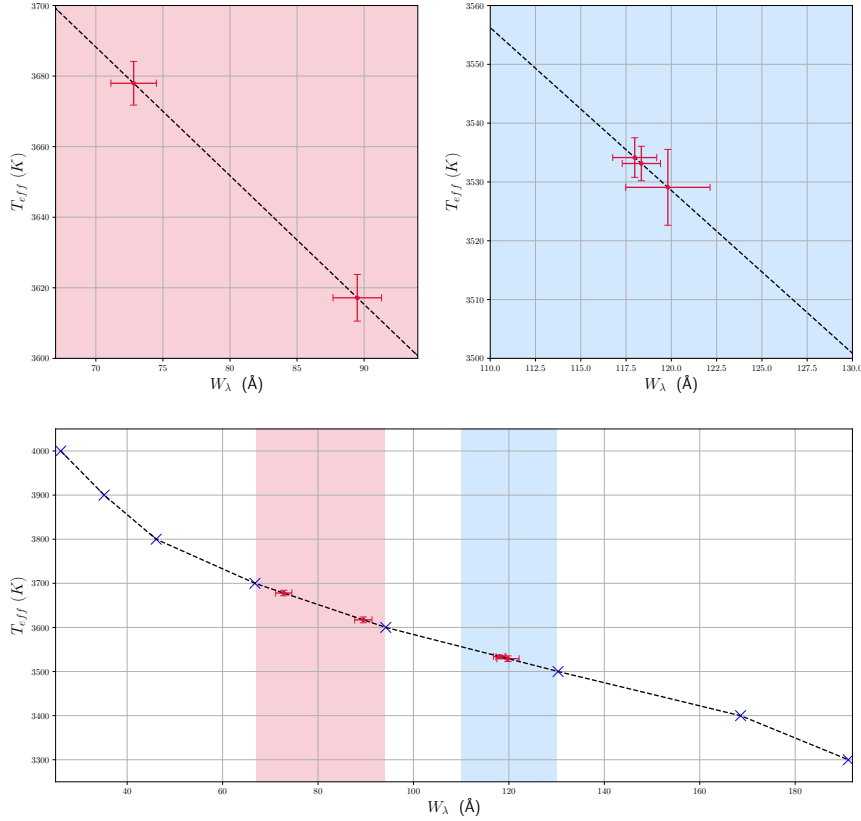


Figure 3.3. The W_λ of Betelgeuse’s 7054 Å TiO absorption feature, shown in red, fit to the relation between the W_λ of the 7054 Å TiO absorption band and T_{eff} derived in §2.5 from synthetic PHOENIX model spectra.

event. For each epoch, the normalized 7054 Å TiO feature is compared to the same feature of a PHOENIX model spectrum of equal T_{eff} . This is accomplished by calculating the weighted arithmetic mean of the same feature for the two model spectrum nearest in T_{eff} . This comparison is shown in Figure 3.1.

3.2 Estimating How V-band Magnitude Changes with Effective Temperature from Models

We investigate if the change in V-band magnitude predicted by the PHOENIX model spectra from the inferred decrease in T_{eff} matches the decline in V-band magnitude observed during the Great Dimming event. Synthetic photometry of the selected grid of PHOENIX model spectra is used to estimate the V-band magnitudes corresponding to the spectra with T_{eff} s ranging from 3300 to 4000 K with a step size of 100 K. The hottest T_{eff} derived from observations is selected as reference temperature T_0 to display the correlation between a decreasing temperature and a decline in V-band magnitude. The change in V-band magnitude estimated by the models (ΔV_{est}) is then compared Betelgeuse's observed change in V-band magnitude (ΔV_{obs}) over the same span of epochs. T_0 is inferred from observations on 2020-04-25. Therefore, ΔT_{eff} and ΔV represent the difference in temperature and V-band magnitude between each individual epoch and 2020-04-25. T_0 is designated $T_0 \equiv 3678$ K. ΔT_{eff} and ΔV are thus defined as follows:

$$\Delta T_{eff} \equiv (T - T_0) \quad \Delta V \equiv (V_T - V_{T_0}) \quad (3.1)$$

Values of ΔT_{eff} inferred from observations are fit to the relation between ΔV and ΔT_{eff} derived from model spectra in §2.6. Figure 3.4 displays the application of the derived ΔV scale to inferred values of ΔT_{eff} . Uncertainties in ΔT_{eff} and ΔV are propagated from the measurements calculated from individual epochs by adding the uncertainties in quadrature. Given n measurements with uncertainties $\sigma_1, \sigma_2, \dots, \sigma_n$, adding in quadrature derives the overall uncertainty σ using the following formula:

$$\sigma = \sqrt{\sigma_1^2 + \sigma_2^2 + \dots + \sigma_n^2} \quad (3.2)$$

As discussed in §3.1, the largest difference in temperature, $\Delta T_{eff} = -149 \pm 12$ K, is seen between the epochs of 2020-02-15 and 2020-04-25. The relation between ΔV and ΔT_{eff} (§2.6) predicts that a decrease in T_{eff} of 149 K would correspond to the V-band magnitude dimming by $\Delta V_{est} = 0.70 \pm 0.04$ mag. Betelgeuse's observed difference in V-band magnitude between the same epochs is $\Delta V_{obs} = 1.13 \pm 0.03$. Values of ΔT_{eff} and correlated estimations of ΔV are shown in Table 3.2. Also included in Table 3.2 are measurements of ΔV derived from photometric observations. The inferred ΔT_{eff} and correlated estimations of ΔV can be seen in comparison to expected values of ΔV in Figure 3.5.

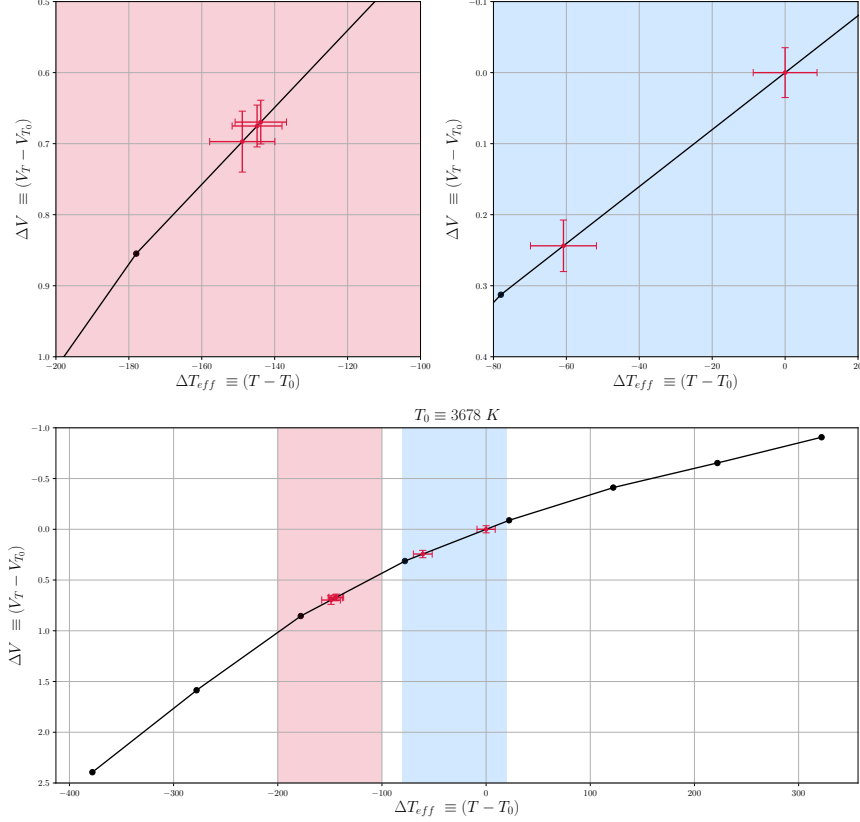


Figure 3.4. Values of ΔV_{est} inferred from Betelgeuse’s ΔT_{eff} , shown in red, fit to ΔV as a function of ΔT_{eff} derived in §2.6 from synthetic PHOENIX model spectra.

Date	ΔT_{eff} (K)	ΔV_{est}	ΔV_{obs}
2020-01-03	-144 ± 10.0	0.67 ± 0.03	0.94 ± 0.04
2020-01-25	-145 ± 9.0	0.68 ± 0.03	1.11 ± 0.03
2020-02-15	-149 ± 12.0	0.70 ± 0.04	1.13 ± 0.03
2020-04-25	0 ± 12.0	0 ± 0.050	0.04 ± 0.00
2021-01-09	-61 ± 13.0	0.40 ± 0.04	0.18 ± 0.04

Table 3.2. Predicted and observed change in V-band magnitude of Betelgeuse before, during, and after the Great Dimming, relative to the fiducial epoch of 2020-04-25. Epoch of observation, temperature difference inferred from the strength of the TiO 7054 Å line(ΔT_{eff}), V-band change predicted by PHOENIX models for the given temperature difference (ΔV_{est}), and actual observed V-band change in Betelgeuse (ΔV_{obs}). Here, $\Delta V \equiv (V_T - V_{T_0})$, $\Delta T_{eff} \equiv (T - T_0)$, and $T_0 \equiv 3678$ K. These results correspond to those presented in Figure 3.4

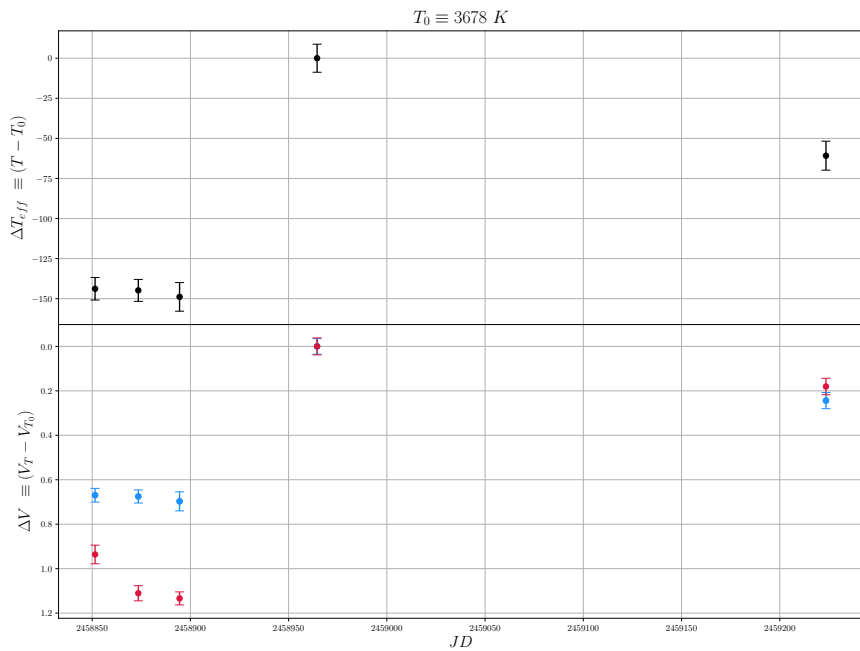


Figure 3.5. Top: Inferred values of Betelgeuse's ΔT_{eff} . Bottom: Changes in Betelgeuse's V-band magnitude ΔV_{est} (shown in blue) derived from the inferred values of ΔT_{eff} . Observed changes in Betelgeuse's V-band magnitude ΔV_{obs} (shown in red) are included for comparison.

CHAPTER 4

Discussion

4.1 Analysis

Our multi-epoch W_λ measurements of Betelgeuse’s 7054 Å TiO absorption feature, derived from spectra obtained during and after the Great Dimming event, demonstrate that the strength of this feature is correlated with Betelgeuse’s luminosity. These results, presented in §3.1, show that as Betelgeuse decreases in brightness, the W_λ of the TiO 7054 Å absorption feature increases. As discussed in Chapter 2, there is an established correlation between the observed strength of the 7054 Å absorption feature and a RSG’s T_{eff} . We investigate the correlation between our W_λ measurements and Betelgeuse’s T_{eff} by comparing our results to the same feature’s W_λ measured over a grid synthetic PHOENIX SEDs with an T_{eff} range of 3300 to 4000 K. W_λ values derived from the PHOENIX SEDs are listed in Table 3.1. This process is described in detail in §2.5.

Furthermore, our results from §3.2 find that as Betelgeuse decreases in brightness, so does its T_{eff} . We interpret these results to suggest that the observed decrease in luminosity observed during the Great Dimming event was indeed accompanied by a decrease in Betelgeuse’s T_{eff} . According to the methods described in §2.6, our inferred decrease of $\Delta T_{eff} = 149 \pm 12$ K predicts a V-band magnitude decline of $\Delta V_{est} = 0.70 \pm 0.04$ mag. However, Betelgeuse’s observed difference in V-band magnitude between the same epochs is $\Delta V_{obs} = 1.13 \pm 0.03$. Figure 3.2 displays our W_λ measurements and the resulting inferred values of T_{eff} with Betelgeuse’s observed V-band magnitude at all epochs, showing that the decrease in luminosity observed during the Great Dimming event is at least partially due to a decreasing surface temperature.

4.2 Comparison with Prior Studies

Numerous studies have proposed hypotheses to explain Betelgeuse’s Great Dimming event. However, the phenomena responsible for the decline in brightness observed between October 2019 and March 2020 and the following swift recovery in luminosity remains contested. We compare our results to the potential scenarios introduced in §1.3, which include: (1) a critical change in the pulsation dynamics suggesting that Betelgeuse is showing early signs of a pre-phase supernova (George

et al. (2020)), (2) strong stellar winds causing fluctuations in the observed color and brightness of Betelgeuse (Davies & Plez (2021)), (3) variations in Betelgeuse’s angular diameter (Dharmawardena et al. (2020)), (4) an interstellar dust cloud not produced by Betelgeuse passing between the star and our line of sight (Levesque & Massey (2020)), (5) an occultation of dust ejected by a recent mass loss event (Dupree et al. (2020); Montargès et al. (2021)), and (6) a drop in Betelgeuse’s T_{eff} localized to a cool patch in the photosphere (potentially linked to a mass loss event) (Harper et al. (2020); Alexeeva et al. (2021); Kravchenko et al. (2021)). A combination of these proposed scenarios has also been suggested in explanation of the dimming event. Of these results, two explanations have gained the most support; an occultation from a newly formed cloud of dust, or a significant decrease in temperature localized to the photosphere’s southern hemisphere. With evidence in support of both scenarios, the cause of the dimming event remains contested, with some in favor of a combination of these two explanations (Levesque & Massey (2020)).

Observations and modeling by Montargès et al. (2021) support the conclusion that a local decrease in temperature ejected a clump of gas, which eventually cooled and formed a large cloud of dust, partially obscuring the star. Though this conclusion links the mass loss event with a temperature decrease, it assumes dust to be the primary cause for the dimming event since the T_{eff} inferred by Levesque & Massey (2020) cannot reproduce the measured decrease in V-band magnitude. In further support of the dust occultation scenario are observations by Dupree et al. (2020), Safonov et al. (2020), and Cotton et al. (2020) which provide evidence to suggest the presence of a large dust cloud near the photosphere of Betelgeuse.

Results from multiple studies contradict the dust occultation hypothesis, suggesting instead that the dimming resulted from a significant fraction of the photosphere having a cooler T_{eff} than normal. Our results appear more consistent with this scenario. From the spectroscopic observations presented in this thesis, we infer a significant decrease in the average surface temperature of Betelgeuse based on the correlation between the observed brightness of the star and the strength of the 7054 Å TiO absorption feature. The results presented in this thesis are consistent with the decrease in T_{eff} corresponding to the dimming event concluded by Harper et al. (2020) and Alexeeva et al. (2021) as well as observations provided by Kravchenko et al. (2021) showing that a localized cool patch appeared on the photosphere (discussed in §1.3).

Though no signatures of dust are detected by Harper et al. (2020) and Gehrzi et al. (2020), conflicting observations by Dupree et al. (2020), Safonov et al. (2020), and Cotton et al. (2020) show evidence of dust surrounding the photosphere by noting an

enhancement in Mg II emission. Harper et al. (2020) reconciles these discrepancies by showing that these observations can be reproduced by either an ejection of hot plasma or changes in the distribution of dust already present near the photosphere (Kervella et al. (2009)). The fact that Levesque & Massey (2020) derive a temperature change of only ~ 50 K whereas we find $\Delta T_{eff} = 149 \pm 12$ K may be due to the lower sensitivity displayed by TiO bands in their spectral range of 4000-6700 Å.

These combined observations and models support the conclusion that the Great Dimming event of Betelgeuse was primarily due to a localized drop in T_{eff} , which is consistent with the results of Dharmawardena et al. (2020) that confirm the dimming of event can result from a localized cool patch in the photosphere. We interpret that our reported temperature decrease of $\Delta T_{eff} = -149 \pm 12.0$ K suggests that an occultation of large dust grains is not the main source of the dimming. Though our reported temperature decrease of $\Delta T_{eff} = 149 \pm 12$ cannot fully reproduce the dimming, this can be reconciled with an inhomogeneous photosphere. Modeling by (Harper et al. (2020)) and (Alexeeva et al. (2021)) show that the observed decreases in luminosity and V-band magnitude can be reproduced without the presence of dust if the southern hemisphere of Betelgeuse was cooler than the northern hemisphere by $\Delta T \geq 250K$. This is consistent with observations of Betelgeuse's surface by Montargès et al. (2021) (Figure 1.10) which show a large dark spot on the star's southern hemisphere. While we cannot completely discount the role of dust, our results provide evidence to suggest that the primary cause of the dimming event was a large portion of the southern hemisphere having a cooler T_{eff} than usual.

CHAPTER 5

Conclusion

Investigating the origin behind the Great Dimming of Betelgeuse is the primary motivation of this thesis. We present five epochs of optical spectra of Betelgeuse observed at Mount Laguna Observatory during and post dimming. Our spectroscopic analysis measures the temperature sensitive 7054 Å TiO absorption feature's W_λ for the first time, and reveals that the strength of this band and Betelgeuse's luminosity are correlated. We derive a scale that correlates the W_λ 7054 Å TiO absorption band to T_{eff} by fitting a 1-D linear interpolation to W_λ values measured over a grid of synthetic PHOENIX SEDs ranging from 3300 to 4000 K. For each epoch, we infer an T_{eff} for Betelgeuse by comparing our W_λ measurements to the derived T_{eff} scale. Our results suggest that Betelgeuse decreased in temperature by at least $T_{eff} = 149 \pm 12$ K during the dimming event, which predicts a V-band magnitude decline of $\Delta V_{est} = 0.70 \pm 0.04$ mag over this same time period. While our results do not completely explain the observed V-band magnitude decline of $\Delta V_{obs} = 1.13 \pm 0.03$ the strong correlation suggests a causal relationship. Furthermore, the results of Harper et al. (2020); Alexeeva et al. (2021); Kravchenko et al. (2021) show that the observed dimming could be explained if the southern hemisphere of Betelgeuse was cooler than the northern hemisphere by $\Delta T \geq 250$ K. We suggest a large portion of the southern photosphere cooled, driving the globally averaged temperature derived through our analysis (of the unresolved Betelgeuse) to drop less precipitously. Since a large portion of the southern hemisphere had a much cooler T_{eff} under this scenario than usual, Betelgeuse's brightness declined, resulting in the Great Dimming Event.

5.1 Limitations of this Study and Future Work

The conclusions drawn by this thesis, along with all spectroscopic studies mentioned, rely on the use of synthetic models to produce accurate T_{eff} calculations. However, results published by Davies & Plez (2021) suggest that current synthetic model spectra fail to account for the strong stellar winds that RSGs produce. These results question the accuracy of T_{eff} diagnostics which rely on TiO features showing that stellar winds can increase the strength of TiO this feature even if the star's T_{eff} remains constant. The results of this thesis, as well as many other similar studies, hinge

on the accuracy of these models. It is difficult for our results to dismiss the claim that this behavior is a result of strong stellar winds without applying our data and methods described in this thesis to models with accurate depictions of stellar winds. Improving stellar models to accurately represent the observed mass loss behavior in these stars is a clear priority for RSG studies in the future. Addressing these concerns will provide further confidence in determining the cause of Betelgeuse's mysterious dimming.

BIBLIOGRAPHY

- Alexeeva, S., Zhao, G., Gao, D.-Y., et al. 2021, Nat Commun, 12, 4719, doi: 10.1038/s41467-021-25018-3
- Allard, F., & Hauschildt, P. H. 1995, The Astrophysical Journal, 445, 433, doi: 10.1086/175708
- Babusiaux, C., Leeuwen, F. v., Barstow, M. A., et al. 2018, A&A, 616, A10, doi: 10.1051/0004-6361/201832843
- Bertre, T. L., Matthews, L. D., Gérard, E., & Libert, Y. 2012, Monthly Notices of the Royal Astronomical Society, 422, 3433, doi: 10.1111/j.1365-2966.2012.20853.x
- Bessell, M. 1999, PUBL ASTRON SOC PAC, 111, 1426, doi: 10.1086/316454
- Bessell, M. S. 1990, Publications of the Astronomical Society of the Pacific, 102, 1181, doi: 10.1086/132749
- . 2005, Annu. Rev. Astron. Astrophys., 43, 293, doi: 10.1146/annurev.astro.41.082801.100251
- Bessell, M. S., Castelli, F., & Plez, B. 1998, Astronomy and Astrophysics, 333, 231. <https://ui.adsabs.harvard.edu/abs/1998A&A...333..231B/abstract>
- Carroll, B. W., & Ostlie, D. A. 2006, An introduction to modern astrophysics and cosmology. <https://ui.adsabs.harvard.edu/abs/2006ima..book.....C>
- Cotton, D. V., Bailey, J., De Horta, A. Y., Norris, B. R. M., & Lomax, J. R. 2020, Research Notes of the American Astronomical Society, 4, 39, doi: 10.3847/2515-5172/ab7f2f
- Davies, B., & Beasor, E. 2020, Monthly Notices of the Royal Astronomical Society: Letters, 496, L142, doi: 10.1093/mnrasl/slaa102
- Davies, B., & Plez, B. 2021, Monthly Notices of the Royal Astronomical Society, stab2645, doi: 10.1093/mnras/stab2645
- Davies, B., Kudritzki, R.-P., Plez, B., et al. 2013, ApJ, 767, 3, doi: 10.1088/0004-637X/767/1/3
- Davis, J. 1997, 189, 31. <http://adsabs.harvard.edu/abs/1997IAUS..189...31D>

- Dharmawardena, T. E., Mairs, S., Scicluna, P., et al. 2020, The Astrophysical Journal, 897, L9, doi: 10.3847/2041-8213/ab9ca6
- Dicenzo, B., & Levesque, E. M. 2019, The Astronomical Journal, 157, 167, doi: 10.3847/1538-3881/ab01cb
- Dolan, M. M., Mathews, G. J., Lam, D. D., et al. 2016, ApJ, 819, 7, doi: 10.3847/0004-637X/819/1/7
- Dupree, A. K., Strassmeier, K. G., Matthews, L. D., et al. 2020, 899, 68, doi: 10.3847/1538-4357/aba516
- Filippenko, A. V. 1982, Publications of the Astronomical Society of the Pacific, 94, 715, doi: 10.1086/131052
- Fuller, J. 2017, Monthly Notices of the Royal Astronomical Society, 470, 1642, doi: 10.1093/mnras/stx1314
- Gehrz, R. D., Marchetti, J., McMillan, S., et al. 2020, The Astronomer's Telegram, 13518, 1. <https://ui.adsabs.harvard.edu/abs/2020ATel13518....1G>
- George, S. V., Kachhara, S., Misra, R., & Ambika, G. 2020, arXiv:2006.16086 [astro-ph]. <http://arxiv.org/abs/2006.16086>
- Goldberg, L. 1984, PASP, 96, 366, doi: 10.1086/131347
- Guinan, E., Wasatonic, R., Calderwood, T., & Carona, D. 2020, The Astronomer's Telegram, 13512, 1. <https://ui.adsabs.harvard.edu/abs/2020ATel13512....1G>
- Guinan, E. F., Wasatonic, R. J., & Calderwood, T. J. 2019, The Astronomer's Telegram, 13341, 1. <https://ui.adsabs.harvard.edu/abs/2019ATel13341....1G>
- Gustafsson, B., Edvardsson, B., Eriksson, K., et al. 2003, 288, 331. <https://ui.adsabs.harvard.edu/abs/2003ASPC..288..331G>
- Hamacher, D. W. 2018, Aust J Anthropol, 29, 89, doi: 10.1111/taja.12257
- Harbaugh, J. 2015, Chandra X-ray Observatory. http://www.nasa.gov/mission_pages/chandra/main/index.html
- Harper, G. M., Brown, A., & Guinan, E. F. 2008, The Astronomical Journal, 135, 1430, doi: 10.1088/0004-6256/135/4/1430

Harper, G. M., Brown, A., Guinan, E. F., et al. 2017, AJ, 154, 11, doi:
 10.3847/1538-3881/aa6ff9

Harper, G. M., Guinan, E. F., Wasatonic, R., & Ryde, N. 2020, ApJ, 905, 34, doi:
 10.3847/1538-4357/abc1f0

Hauschildt, P. H., Allard, F., Ferguson, J., Baron, E., & Alexander, D. R. 1999, The
 Astrophysical Journal, 525, 871, doi: 10.1086/307954

Heffner, C. M. . 2012, Master's thesis, San Diego State University

Husser, T.-O., von Berg, S. W., Dreizler, S., et al. 2013, A&A, 553, A6, doi:
 10.1051/0004-6361/201219058

Johnson, S. A., Kochanek, C. S., & Adams, S. M. 2018, Monthly Notices of the Royal
 Astronomical Society, 480, 1696, doi: 10.1093/mnras/sty1966

Josselin, E., & Plez, B. 2007, A&A, 469, 671, doi: 10.1051/0004-6361:20066353

Joyce, M., Leung, S.-C., Molnár, L., et al. 2020, arXiv:2006.09837 [astro-ph].
<http://arxiv.org/abs/2006.09837>

Keenan, P. C., & McNeil, R. C. 1989, The Astrophysical Journal Supplement Series, 71,
 245, doi: 10.1086/191373

Kervella, P., Verhoelst, T., Ridgway, S. T., et al. 2009, A&A, 504, 115, doi:
 10.1051/0004-6361/200912521

Kiss, L. L., Szabo, G. M., & Bedding, T. R. 2006, Monthly Notices of the Royal
 Astronomical Society, 372, 1721, doi: 10.1111/j.1365-2966.2006.10973.x

Kravchenko, K., Jorissen, A., Van Eck, S., et al. 2021, A&A, 650, L17, doi:
 10.1051/0004-6361/202039801

Leaman, T. M., & Hamacher, D. W. 2014, arXiv:1403.7849 [physics].
<http://arxiv.org/abs/1403.7849>

Leavitt, H. S., & Pickering, E. C. 1912, Harvard College Observatory Circular, 173, 1.
<https://ui.adsabs.harvard.edu/abs/1912HarCi.173....1L>

LeBlanc, F. 2010, An Introduction to Stellar Astrophysics.
<https://ui.adsabs.harvard.edu/abs/2010isa..book.....L>

- Ledrew, G. 2001, Journal of the Royal Astronomical Society of Canada, 95, 32.
<https://ui.adsabs.harvard.edu/abs/2001JRASC..95...32L>
- Leonard, D. C., Filippenko, A. V., Barth, A. J., & Matheson, T. 2000, ApJ, 536, 239,
doi: 10.1086/308910
- Levesque, E. M. 2010, New Astronomy Reviews, 54, 1, doi:
10.1016/j.newar.2009.10.002
- . 2017, Astrophysics of Red Supergiants, doi: 10.1088/978-0-7503-1329-2
- Levesque, E. M., & Massey, P. 2020, ApJ, 891, L37, doi: 10.3847/2041-8213/ab7935
- Levesque, E. M., Massey, P., Olsen, K. A. G., et al. 2005, ApJ, 628, 973, doi:
10.1086/430901
- Levesque, E. M., Massey, P., Olsen, K. a. G., et al. 2006, ApJ, 645, 1102, doi:
10.1086/504417
- Lloyd, C. 2020, arXiv:2006.15403 [astro-ph]. <http://arxiv.org/abs/2006.15403>
- Mack, E. 2020, Giant star Betelgeuse might explode soon, and the next few weeks are critical. <https://www.cnet.com/science/huge-red-star-might-explode-soon-and-next-few-weeks-are-critical/>
- Massey, P. 1998, ApJ, 501, 153, doi: 10.1086/305818
- Matheson, T., Filippenko, A. V., Barth, A. J., et al. 2000, AJ, 120, 1487, doi:
10.1086/301518
- Mathias, P., Aurière, M., Ariste, A. L., et al. 2018, A&A, 615, A116, doi:
10.1051/0004-6361/201732542
- Meynet, G., Haemmerlé, L., Ekström, S., et al. 2013, EAS Publications Series, 60, 17,
doi: 10.1051/eas/1360002
- Montargès, M., Cannon, E., Lagadec, E., et al. 2021, Nature, 594, 365, doi:
10.1038/s41586-021-03546-8
- Mészáros, S., & Prieto, C. A. 2013, Monthly Notices of the Royal Astronomical Society, 430, 3285, doi: 10.1093/mnras/stt130
- Neilson, H., Lester, J. B., & Haubois, X. 2011, arXiv:1109.4562 [astro-ph].
<http://arxiv.org/abs/1109.4562>

- O'Gorman, E., Harper, G. M., Ohnaka, K., et al. 2020, A&A, 638, A65, doi: 10.1051/0004-6361/202037756
- Ohnaka, K., Weigelt, G., Millour, F., et al. 2011, A&A, 529, A163, doi: 10.1051/0004-6361/201016279
- Perryman, M. A. C., Mission, H., & Agency, E. S., eds. 1997, The Hipparcos and tycho catalogues: astrometric and photometric star catalogues derived from the ESA Hipparcos Space Astronometry Mission, medienkombination edn., ESA SP No. 1200 (Noordwijk: ESA Publ. Div., c/o ESTEC)
- Quataert, E., & Shiode, J. 2012, Monthly Notices of the Royal Astronomical Society, 423, L92, doi: 10.1111/j.1745-3933.2012.01264.x
- Safonov, B., Dodin, A., Burlak, M., et al. 2020, arXiv:2005.05215 [astro-ph].
<http://arxiv.org/abs/2005.05215>
- Schaefer, B. E. 2018, Journal of Astronomical History and Heritage, 21, 7.
<https://ui.adsabs.harvard.edu/abs/2018JAHH...21....7S>
- Schwarzschild, M. 1975, The Astrophysical Journal, 195, 137, doi: 10.1086/153313
- Sigismundi, C. 2020, Gerbertvs, International Academic Publication on History of Medieval Science, 13, 39.
<https://ui.adsabs.harvard.edu/abs/2020Gerb...13...39S>
- Smith, C. E., & Nelson, B. 1969, PASP, 81, 74, doi: 10.1086/128742
- Smith, N., & Arnett, W. D. 2014, The Astrophysical Journal, 785, 82, doi: 10.1088/0004-637X/785/2/82
- Stothers, R. 1969, The Astrophysical Journal, 156, 541, doi: 10.1086/149987
—. 1972, Astronomy and Astrophysics, 18, 325.
<https://ui.adsabs.harvard.edu/abs/1972A&A....18..325S/abstract>
- Stothers, R. B. 2010, ApJ, 725, 1170, doi: 10.1088/0004-637X/725/1/1170
- Straizys, V. 1996, Baltic Astronomy, 5, 459, doi: 10.1515/astro-1996-0308
- Townes, C. H., Wishnow, E. H., Hale, D. D. S., & Walp, B. 2009, ApJ, 697, L127, doi: 10.1088/0004-637X/697/2/L127

van Altena, W. F., Lee, J. T., & Hoffleit, D. 1995, VizieR Online Data Catalog, I/174.
<https://ui.adsabs.harvard.edu/abs/1995yCat.1174....0V>

van Leeuwen, F. 2007, Astrophysics and Space Science Library, 350, doi:
10.1007/978-1-4020-6342-8

Vollmann, K., & Eversberg, T. 2006, Astron. Nachr., 327, 862, doi:
10.1002/asna.200610645

Wade, R. A., & Horne, K. 1988, The Astrophysical Journal, 324, 411, doi:
10.1086/165905

Weiner, J., Hale, D. D. S., & Townes, C. H. 2003, ApJ, 589, 976, doi: 10.1086/374779

Woosley, S. E., & Heger, A. 2015, The Astrophysical Journal, 810, 34, doi:
10.1088/0004-637X/810/1/34

APPENDIX
Additional Figures

Additional Figures

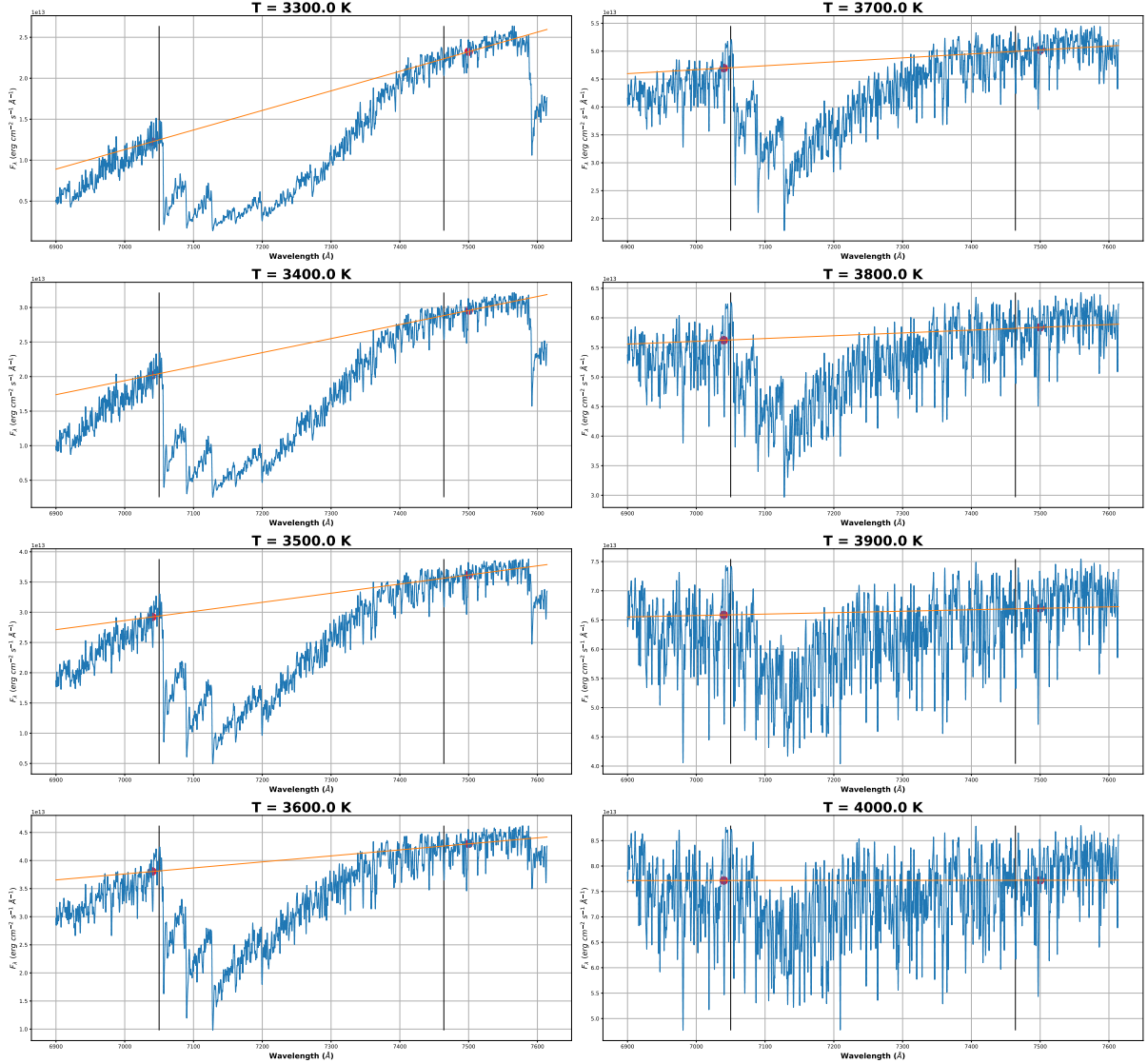


Figure A.1. Continuum estimates of the 7054 \AA TiO band in all selected PHOENIX synthetic spectra, ranging from 3300 – 4000 Kelvin.

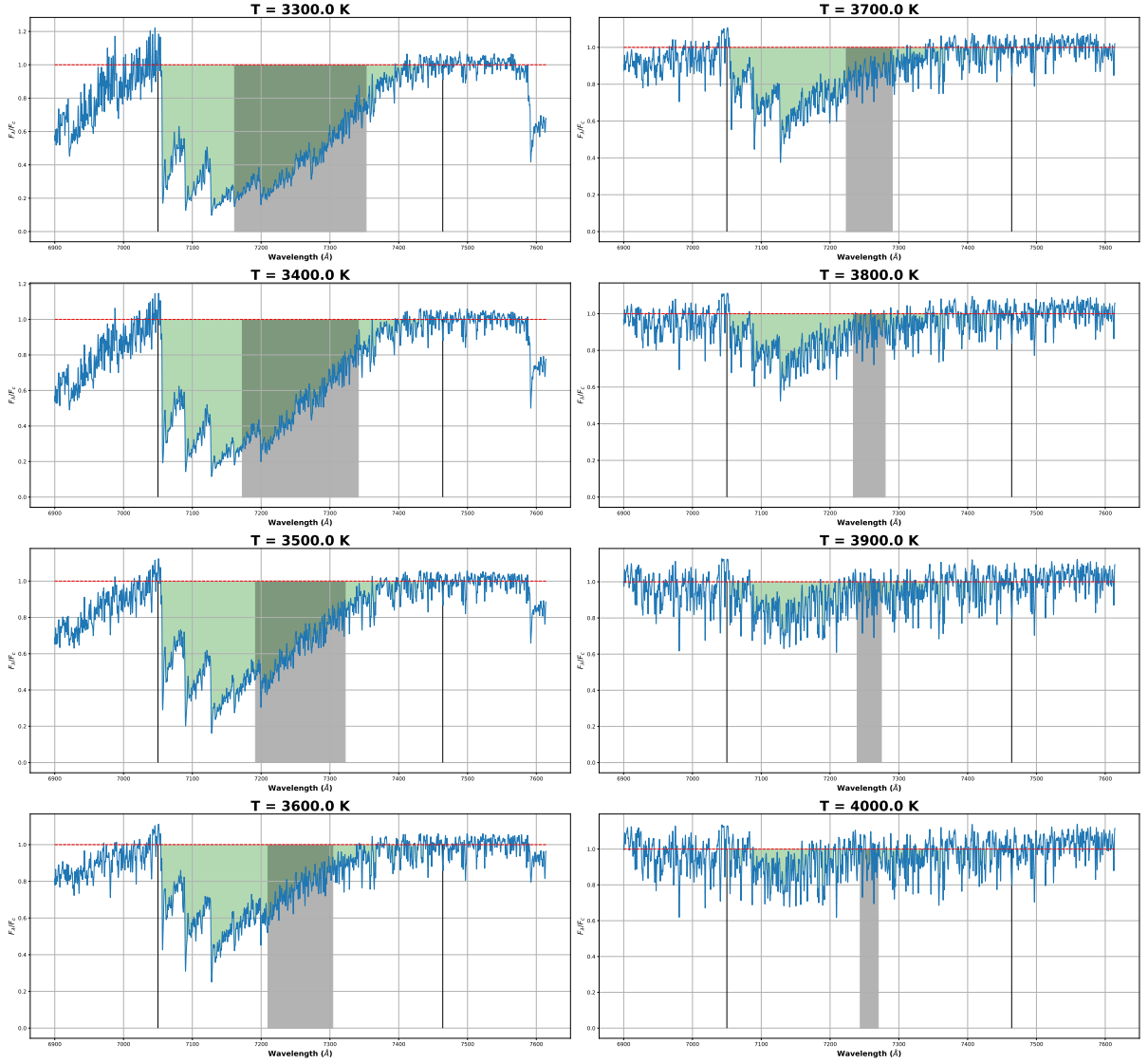


Figure A.2. Normalized continuum profiles for the 7054 Å TiO band in all selected PHOENIX synthetic spectra, ranging from 3300 – 4000 Kelvin. The horizontal width of the grey shaded area corresponds to the measured W_λ . The shaded grey area has the same area as the line strength, shown in green.